Clarifying the Relation between AMOC and Thermal Wind: Application to the Centennial Variability in a Coupled Climate Model

Robin Waldman, Joël Hirschi, Aurore Voldoire, Christophe Cassou, Rym Msadek

Clarifying the Relation between AMOC and Thermal Wind: Application to the Centennial Variability in a Coupled Climate Model

ROBIN WALDMAN,[a] JOËL HIRSCHI,[b] AURORE VOLDOIRE,[a] CHRISTOPHE CASSOU,[c] AND RYM MSADEK[c]

[a] *Centre National de Recherches Météorologiques, Toulouse, France*
[b] *National Oceanographic Centre, Southampton, United Kingdom*
[c] *CECI, Université de Toulouse, CNRS, CERFACS, Toulouse, France*

(Manuscript received 25 November 2019, in final form 9 October 2020)

ABSTRACT: This work aims to clarify the relation between the Atlantic meridional overturning circulation (AMOC) and the thermal wind. We derive a new and generic dynamical AMOC decomposition that expresses the thermal wind transport as a simple vertical integral function of eastern minus western boundary densities. This allows us to express density anomalies at any depth as a geostrophic transport in Sverdrups ($1\,\text{Sv} \equiv 10^6\,\text{m}^3\,\text{s}^{-1}$) per meter and to predict that density anomalies around the depth of maximum overturning induce most AMOC transport. We then apply this formalism to identify the dynamical drivers of the centennial AMOC variability in the CNRM-CM6 climate model. The dynamical reconstruction and specifically the thermal wind component explain over 80% of the low-frequency AMOC variance at all latitudes, which is therefore almost exclusively driven by density anomalies at both zonal boundaries. This transport variability is dominated by density anomalies between depths of 500 and 1500 m, in agreement with theoretical predictions. At those depths, southward-propagating western boundary temperature anomalies induce the centennial geostrophic AMOC transport variability in the North Atlantic. They are originated along the western boundary of the subpolar gyre through the Labrador Sea deep convection and the Davis Strait overflow.

KEYWORDS: Ocean; Atlantic Ocean; Meridional overturning circulation; Climate models; Multidecadal variability

1. Introduction

The Atlantic meridional overturning circulation (AMOC) defines the zonally integrated Eulerian mean circulation in the meridional plane over the Atlantic Ocean. At its main observation site, in the subtropical North Atlantic Ocean (26.5°N), it displays two main overturning cells, an upper cell (above typically 4000-m depth) of magnitude 17.2 Sv ($1\,\text{Sv} \equiv 10^6\,\text{m}^3\,\text{s}^{-1}$) associated with the formation and subsequent southward transport of the North Atlantic Deep Water (NADW) and a much weaker (~ -2 Sv) bottom cell related to the northward transport and transformation of the Antarctic Bottom Waters (AABW) (McCarthy et al. 2015). The upper cell, tightly related to the formation of deep waters in the subpolar North Atlantic (Buckley and Marshall 2016), largely dominates the oceanic meridional heat transport by advecting warm upper-limb (typically upper 1000 m) waters northward and colder lower-limb waters southward, causing a net northward heat transport at all latitudes (Ganachaud and Wunsch 2003; Trenberth and Fasullo 2017). Therefore, the AMOC has long been believed to regulate the climate of the Atlantic Ocean and adjacent continents (Zhang et al. 2019).

However, the relation between the AMOC variability and surface climate fluctuations is not evident in observations due to the very limited measurements of the former. So far, it can only be investigated with paleoclimatic proxies, which suggest that such a link exists (Stocker 1998; Clark et al. 2002), and with coupled climate models. Over the last two decades, an ever-increasing number of numerical studies have analyzed the relation between the AMOC and the climate of the Atlantic region (e.g., Ruprich-Robert and Cassou (2015) and Cassou et al. (2018), and references therein). The ocean circulation forces the atmosphere mostly by modulating, as a result of transport and mixing processes, the sea surface temperature (SST), which in turn modulates air–sea heat, momentum, and water fluxes. The AMOC is one of those drivers, and its anomalies are generally found to lead a sea surface temperature anomaly consistent with the anomalous heat transport (Buckley and Marshall 2016). It is believed to be a major driver of decadal to centennial SST variability (Muir and Fedorov 2015), and although the related atmospheric response is generally weak (e.g., Gastineau and Frankignoul 2012), it can be interpreted as one of the dominant modes of internal climate variability at those time scales (Kushnir 1994). In particular, recent studies have shown that the AMOC has predictive skills at the decadal time scale (Desbruyères et al. 2019), which provides some skill for the decadal prediction of SST over the subpolar North Atlantic and Greenland–Icelandic and Norwegian (GIN) Seas (Yeager and Robson 2017).

Because of presence of intense peaks in the AMOC low-frequency spectrum of long climate simulations, this variability cannot simply be a "red noise" signal resulting from the temporal integration of some stochastic atmospheric forcing (e.g., a first-order autoregressive process; Frankignoul and Hasselmann 1977).

Denotes content that is immediately available upon publication as open access.

Supplemental information related to this paper is available at the Journals Online website: https://doi.org/10.1175/JPO-D-19-0284.s1.

Corresponding author: Robin Waldman, robin.waldman@meteo.fr

DOI: 10.1175/JPO-D-19-0284.1

Hence it is accepted that oceanic dynamical processes impose an AMOC variability at specific frequencies (Frankignoul et al. 1997). Statistically, this behavior can be reasonably well fitted to a "delayed oscillator" model in which an ocean feedback delay term is added to the red-noise model, which accounts for internal oscillations driven by ocean dynamics (Tulloch and Marshall 2012). However, no consensus has emerged either on the dominant time scales or on the nature of the forcing and the internal oscillation mechanism that, altogether, give rise to the AMOC low-frequency spectral peaks (Menary et al. (2015) and references therein).

Only one constraint is commonly accepted, which stems from the thermal wind relation: all those drivers must ultimately manifest themselves as a zonally integrated density gradient (Hirschi and Marotzke 2007; Tulloch and Marshall 2012). Indeed, at any latitude density anomalies at the western and eastern boundaries of the Atlantic Ocean drive the geostrophic component of the AMOC, which is believed to dominate its low-frequency variability (Buckley and Marshall 2016). The very accurate geostrophic approximation in the interior ocean has permitted the design of the RAPID array, which was the first continuous AMOC monitoring program (Hirschi et al. 2003; Baehr et al. 2004; Rayner et al. 2011). Most studies relating the AMOC to this zonally integrated thermal wind put forward the dominant role of western boundary density anomalies in driving the low-frequency AMOC variability.

The thermal wind relation requires a reference level of integration that implies a formal separation between barotropic (viz., depth-independent) and baroclinic (viz., depth-dependent) contributions. In addition, deducing a vertically integrated transport requires a double vertical integration of density gradients, first to retrieve geostrophic velocities and then to integrate the transport (e.g., Lee and Marotzke 1998; Sime et al. 2006; Hirschi and Marotzke 2007; Cabanes et al. 2008; Köhl and Stammer 2008; Tulloch and Marshall 2012). This has limited our understanding of the relationship between zonal density gradients and the AMOC.

The aim of the present study is twofold: first to reformulate an AMOC decomposition that clarifies the contribution of the zonally integrated density gradient; and then to investigate the low-frequency AMOC variability in the latest generation of the CNRM-CM coupled climate model (hereinafter CNRM-CM6; Voldoire et al. 2019). For that, we formulate in section 2 a new AMOC decomposition that clarifies the contributions of density anomalies at the zonal boundaries. We then make use of this decomposition in section 3 to identify the geostrophic driver of the strong centennial AMOC variability found in the CNRM-CM6 model. In section 4, we relate this geostrophic AMOC driver to the sources of dense water variability in the North Atlantic subpolar region.

2. Relation between the AMOC and zonal density anomalies

a. AMOC definition and decomposition

For the remainder of this paper the term AMOC will refer to the vertical maximum of the Eulerian mean meridional overturning streamfunction $\Psi(y, z, t)$ (see section SI1 in the online supplemental material for a discussion on the residual mean overturning streamfunction). This streamfunction is defined as

$$\Psi(y,z,t) = \int_{z}^{0}\int_{x_W}^{x_E} v(x,y,z',t)\,dx\,dz', \tag{1}$$

where x_W and x_E are the western and eastern boundaries, v is the meridional velocity, and z' is the variable of vertical integration and neglecting sea level. The AMOC is then

$$\begin{aligned}\mathrm{AMOC}(y,t) &= \Psi[y, z_m(y,t), t]\\ &= \int_{z_m(y,t)}^{0}\int_{x_W}^{x_E} v(x,y,z,t)\,dx\,dz,\end{aligned} \tag{2}$$

with $z_m < 0$ being the depth of maximum overturning. It quantifies the total northward volume transport associated with the upper limb of the main meridional overturning cell in the Atlantic. This definition corresponds to the depth coordinate AMOC, as opposed to the density coordinate AMOC. As discussed in section SI2 of the online supplemental material, the latter has no simple expression as a function of hydrographic properties at the boundaries because the interface depth is a zonally variable isopycnal depth. Therefore, we focus in this study on the vertical coordinate AMOC. Although z_m can be chosen to be variable in time and latitude, in the following we will consider the time and latitude average depth of maximum overturning over the Atlantic Ocean (30°S–60°N). Henceforth, we only mention dependency on space and time when relevant.

Over scales longer than a few days and outside the deep tropics (within ~2° of the equator, excluded in what follows), the AMOC can be approximated by Ekman plus geostrophic dynamics (e.g., Baehr et al. 2004):

$$\begin{aligned}\mathrm{AMOC} &\simeq \mathrm{AMOC}_E + \mathrm{AMOC}_g\\ &= \int_{z_m}^{0}\int_{x_W}^{x_E} (v_E + v_g)\,dx\,dz,\end{aligned} \tag{3}$$

with v_E and v_g being the Ekman and geostrophic velocities. Table 1 summarizes all of the physical AMOC decompositions used in this work. The vertically integrated Ekman transport is given by Ekman theory as

$$\begin{aligned}V_E &= \int_{-h_E}^{0} v_E\,dz\\ &= -\frac{\tau_x}{\rho_0 f},\end{aligned} \tag{4}$$

where h_E is the Ekman depth restricted to the upper limb ($h_E \ll -z_m$), τ_x is the surface zonal wind stress, ρ_0 is a reference average density, and f is the Coriolis parameter. Geostrophic transports result both from the surface pressure gradient due to sea level variations and the hydrostatic pressure gradient due to density variations within the water column. However, both terms generally compensate each other at depth so that bottom velocities are much reduced compared to surface currents. Therefore, it is simpler and more convenient to deduce geostrophic currents from the thermal wind relation, which combines the geostrophic and hydrostatic balances:

$$\frac{\partial v_g}{\partial z} = -\frac{g}{\rho_0 f}\frac{\partial \rho}{\partial x}, \tag{5}$$

TABLE 1. Decompositions, reference equation, and physical interpretation for the total AMOC, its geostrophic shear contribution ($AMOC_{g-sh}$), and the thermal wind transport per unit depth [$TW(z)$].

Decomposition	Formula	Physical interpretation
		AMOC
$AMOC_E + AMOC_g$	Eq. (3)	Ekman plus geostrophic AMOC decomposition: $AMOC_E$ is Ekman component; $AMOC_g$ is geostrophic component
$AMOC_E + AMOC_{BCg} + AMOC_{BTg}$	Eq. (7)	Use of the thermal wind relation to decompose the geostrophic AMOC into baroclinic and a barotropic contributions: $AMOC_{BTg}$ is barotropic geostrophic AMOC transport related to the reference velocities used for the thermal wind integration (in this study, bottom velocities); $AMOC_{BCg}$ is baroclinic geostrophic AMOC transport related to velocity anomalies with respect to the reference depth velocities
$AMOC_{E-sh} + AMOC_{g-sh}$	Eq. (12)	Use of the no-net-integral-flow condition to include the barotropic geostrophic transport as a compensation within the Ekman and baroclinic geostrophic components: $AMOC_{E-sh}$ is sheared Ekman component including the barotropic compensation that ensures no net integral transport; $AMOC_{g-sh}$ is sheared geostrophic component including the barotropic compensation that ensures no net integral transport
$AMOC_{E-sh} + AMOC_{g-sh} + AMOC_{g-EM}$	Eq. (19)	Inclusion of the external mode with variable topography: $AMOC_{g-EM}$ is external-mode AMOC transport induced by variable bottom velocities over variable topography and upper-limb depth
		$AMOC_{g-sh}$
$\int_{-h}^{0} TW(z)\,dz$	Eqs. (15) and (16)	Expression of the $AMOC_{g-sh}$ as a single vertical integral: $TW(z)$ is thermal wind transport per unit depth ($Sv\,m^{-1}$) caused by density differences at both zonal boundaries
$AMOC_{gT-sh} + AMOC_{gS-sh}$	Eq. (22)	Decomposition into thermal and haline contributions: $AMOC_{gT-sh}$ is geostrophic shear AMOC transport due to temperature differences at both zonal boundaries; $AMOC_{gS-sh}$ is geostrophic shear AMOC transport due to salinity differences at both zonal boundaries
$AMOC_{gW-sh} + AMOC_{gE-sh}$	Eq. (24)	Decomposition into western and eastern boundary contributions (only meaningful in anomaly with respect to a mean state): $AMOC_{gW-sh}$ is geostrophic shear AMOC transport due to density anomalies at the western boundary; $AMOC_{gE-sh}$ is geostrophic shear AMOC transport due to density anomalies at the eastern boundary
		$TW(z)$
$TW_T(z) + TW_S(z)$	Eq. (22)	Decomposition into thermal and haline contributions: $TW_T(z)$ is thermal wind transport due to temperature differences between both zonal boundaries; $TW_S(z)$ is thermal wind transport due to salinity differences between both zonal boundaries
$TW_W(z) + TW_E(z)$	Eq. (24)	Decomposition into western and eastern boundary contributions (only meaningful in anomaly with respect to a mean state): $TW_W(z)$ is thermal wind transport due to density anomalies at the western boundary; $TW_E(z)$ is thermal wind transport due to density anomalies at the eastern boundary

with g being the gravity acceleration and ρ being the seawater in situ density. Integrating vertically from the ocean bottom depth $-h$ (with $h > 0$) gives

$$v_g(z) = v_g(-h) - \frac{g}{\rho_0 f}\int_{-h}^{z}\frac{\partial \rho}{\partial x}dz', \tag{6}$$

with $v_g(-h)$ being the bottom geostrophic velocity. In what follows, $v_g(-h)$ is referred to as the barotropic component because it does not depend on depth, whereas the second term depends on the density profile and is named the baroclinic component. For simplicity we first consider a rectangular basin with constant depth. The AMOC is then (Table 1)

$$\begin{aligned}\mathrm{AMOC} &= -\frac{1}{\rho_0 f}\int_{x_W}^{x_E}\tau_x\,dx + \int_{z_m}^{0}\int_{x_W}^{x_E}\left[v_g(-h) - \frac{g}{\rho_0 f}\int_{-h}^{z}\frac{\partial \rho}{\partial x}dz'\right]dx\,dz\\ &= -\frac{\Delta x}{\rho_0 f}\overline{\tau_x} - z_m\Delta x\overline{v_g(-h)} - \frac{g}{\rho_0 f}\int_{z_m}^{0}\int_{-h}^{z}\Delta\rho\,dz'\,dz\\ &= \mathrm{AMOC}_E + \mathrm{AMOC}_{\mathrm{BTg}} + \mathrm{AMOC}_{\mathrm{BCg}},\end{aligned} \tag{7}$$

with $\Delta x = x_E - x_W$ and $\Delta\rho = \rho(x_E) - \rho(x_W)$ being the basin zonal width and integrated density gradient and the overbar denoting a zonal average over the basin width. AMOC_E is the zonally integrated Ekman transport, $\mathrm{AMOC}_{\mathrm{BTg}}$ is the barotropic upper-limb transport due to bottom geostrophic velocities, and $\mathrm{AMOC}_{\mathrm{BCg}}$ is the baroclinic geostrophic transport due to the basin-integrated zonal density gradient.

b. Baroclinic transport as a simple integral of density

Let us simplify the baroclinic geostrophic transport [last term of Eq. (7)]. So far, it has been expressed as a double vertical integral over depth (as above), which hides the contribution of density anomalies at individual depths to the AMOC (Buckley and Marshall 2016, and references therein). We now use the double integration rule to write this last term as a simple vertical integral of densities:

$$\begin{aligned}\mathrm{AMOC}_{\mathrm{BCg}} &= -\frac{g}{\rho_0 f}\int_{z_m}^{0}\int_{-h}^{z}\Delta\rho(z')\,dz'\,dz\\ &= -\frac{g}{\rho_0 f}\left[\int_{-h}^{z_m}\int_{z_m}^{0}\Delta\rho(z')\,dz\,dz' - \int_{z_m}^{0}\int_{z'}^{0}\Delta\rho(z')\,dz\,dz'\right]\\ &= +\frac{z_m g}{\rho_0 f}\int_{-h}^{z_m}\Delta\rho(z')\,dz' + \frac{g}{\rho_0 f}\int_{z_m}^{0} z'\Delta\rho(z')\,dz'.\end{aligned} \tag{8}$$

We have reversed the order of integration in order to integrate vertically $\Delta\rho(z')$, which depends on the variable of vertical integration of density z' but not on that of vertical integration of velocities z. The first term of Eq. (8) represents baroclinic geostrophic transports due to density anomalies below the depth z_m, which by construction of the baroclinic component affect velocities throughout the upper-limb thickness $-z_m$. The second term relates to density anomalies above the depth z_m, which by construction only affect velocities above the depth z', that is over a fraction of the upper limb.

c. Barotropic transport from mass conservation

Let us now determine the barotropic geostrophic transport [second term of Eq. (7)], which depends on the zonal profile of bottom geostrophic velocities. So far it has been considered separately from the baroclinic contribution (e.g., Hirschi and Marotzke 2007), although both can be combined by mass continuity. Indeed, over scales longer than a few days, the water volume north of any zonal section is reasonably well conserved (Bryden et al. 2009), so that the net northward flow must vanish. We neglect the net transport arising from the small imbalance between Bering Straits transport and the surface water budget north of the latitude considered, which is typically one–two orders of magnitude weaker than the AMOC magnitude (Bryden and Imawaki 2001). This means that

$$\Psi(-h) = \int_{-h}^{0}\int_{x_W}^{x_E}(v_E + v_g)\,dx\,dz \simeq 0. \tag{9}$$

Resolving this equation yields a formulation for the zonally averaged bottom geostrophic velocities, as follows:

$$\begin{aligned}\Psi(-h) &= \mathrm{AMOC}_E + \int_{-h}^{0}\int_{x_W}^{x_E}\left[v_g(-h) - \frac{g}{\rho_0 f}\int_{-h}^{z}\frac{\partial\rho}{\partial x}dz'\right]dx\,dz\\ &= \mathrm{AMOC}_E + h\Delta x\overline{v_g(-h)} + \frac{g}{\rho_0 f}\int_{-h}^{0} z'\Delta\rho(z')\,dz'.\end{aligned} \tag{10}$$

As in Eq. (8), we have used the double integration rule to simplify the last term. In the case of constant bathymetry, this last term times the Coriolis parameter is the baroclinic potential energy difference already used to diagnose Southern Ocean transports (Hughes and Killworth 1995; Borowski et al. 2002; Olbers et al. 2004; Saenko et al. 2005; Böning et al. 2008). It corresponds to the baroclinic geostrophic transport integrated throughout the water column. Hence, we have

$$\Psi(-h) = 0 \Leftrightarrow \overline{v_g(-h)} = -\frac{1}{h\Delta x}\left[\mathrm{AMOC}_E + \frac{g}{\rho_0 f}\int_{-h}^{0} z'\Delta\rho(z')\,dz'\right]. \tag{11}$$

The first term on the right-hand side of Eq. (11) is the geostrophic compensation for the net meridional Ekman transport, which applies to the whole ocean depth because it is barotropic. The second term is the barotropic geostrophic compensation for the baroclinic geostrophic transport, whose net transport does not necessarily cancel out. It does not modify the vertical geostrophic velocity profile, but it ensures that its vertical integration is null. In other words, it ensures that what flows north above z_m depth is exactly equal to what flows south below that depth.

d. AMOC as a simple integral of density

We can finally write the AMOC transport [Eq. (7)] as a simple integral function of density, plus a function of zonal wind stress (Table 1):

$$\begin{aligned}\mathrm{AMOC} &= \mathrm{AMOC}_E + \frac{z_m}{h}\left[\mathrm{AMOC}_E + \frac{g}{\rho_0 f}\int_{-h}^{0} z'\Delta\rho(z')\,dz'\right] + \frac{z_m g}{\rho_0 f}\int_{-h}^{z_m}\Delta\rho(z')\,dz' + \frac{g}{\rho_0 f}\int_{z_m}^{0} z'\Delta\rho(z')\,dz'\\ &= -\left(1+\frac{z_m}{h}\right)\frac{\Delta x}{\rho_0 f}\overline{\tau_x} + \frac{g}{\rho_0 f}\left[\int_{-h}^{z_m} z_m\left(1+\frac{z'}{h}\right)\Delta\rho(z')\,dz' + \int_{z_m}^{0} z'\left(1+\frac{z_m}{h}\right)\Delta\rho(z')\,dz'\right]\\ &= \mathrm{AMOC}_{E-\mathrm{sh}} + \mathrm{AMOC}_{g-\mathrm{sh}},\end{aligned} \tag{12}$$

with

$$\mathrm{AMOC}_{E-\mathrm{sh}} = -\left(1+\frac{z_m}{h}\right)\frac{\Delta x}{\rho_0 f}\overline{\tau_x} = \left(1+\frac{z_m}{h}\right)\mathrm{AMOC}_E \quad \text{and} \tag{13}$$

$$\mathrm{AMOC}_{g-\mathrm{sh}} = \frac{g}{\rho_0 f}\left[\int_{-h}^{z_m} z_m\left(1+\frac{z'}{h}\right)\Delta\rho(z')\,dz' + \int_{z_m}^{0} z'\left(1+\frac{z_m}{h}\right)\Delta\rho(z')\,dz'\right]. \tag{14}$$

$\mathrm{AMOC}_{E-\mathrm{sh}}$ is the sheared (i.e., vertically compensated) Ekman transport. $\mathrm{AMOC}_{g-\mathrm{sh}}$ is the so-called geostrophic shear transport, which is the baroclinic geostrophic AMOC compensated to ensure the no-net-flow condition (Hirschi and Marotzke 2007). Hence, the barotropic geostrophic velocity reduces the contributions of both the Ekman and baroclinic geostrophic velocities to the AMOC. Indeed, to ensure mass conservation, $\mathrm{AMOC}_{\mathrm{BTg}}$ will oppose any AMOC_E or $\mathrm{AMOC}_{\mathrm{BCg}}$ anomaly, of either sign, so that the depth-integrated transport cancels out. Note that both $\mathrm{AMOC}_{E-\mathrm{sh}}$ and $\mathrm{AMOC}_{g-\mathrm{sh}}$ include a fraction of the barotropic geostrophic transport, so that they cannot be considered as purely forced by the wind stress and zonal density anomalies, respectively. However, this decomposition has the convenience of separating the AMOC as a function of zonal wind stress plus a function of the basin-integrated density gradient profile.

To clarify the interpretation, let us consider typical values of $h = 4000$ m and $z_m = -1000$ m. In this case,

- $\mathrm{AMOC}_{\mathrm{BTg}}$ opposes by a factor of 1/4 the Ekman transport: indeed, the vertically integrated barotropic adjustment must be exactly opposed to AMOC_E. The upper limb of AMOC represents only 1/4 of the total depth, so this barotropic adjustment only opposes by 1/4 Ekman transports above z_m [the factor z_m/h of Eq. (13)], with the remaining 3/4 occurring below z_m.
- Similarly, any baroclinic geostrophic transport induced by density anomalies above z_m is reduced by a factor of 1/4 by the barotropic contribution [the factor $1 + (z_m/h)$ within the second integral of Eq. (14)].
- Baroclinic geostrophic transports induced by density anomalies below z_m are reduced by a factor of 1/4–1 depending on the depth of such density anomalies [the factor $1 + (z'/h)$ within the first integral of Eq. (14)]. The deeper the density anomaly is, the larger is the barotropic correction because of an ever-larger vertically integrated baroclinic transport. In the extreme case of a density anomaly at the bottom depth, the baroclinic velocity anomaly is constant with depth, so that the barotropic adjustment exactly cancels it.

e. *Thermal wind transport as a function of depth*

The geostrophic shear AMOC transport [$\mathrm{AMOC}_{g-\mathrm{sh}}$; Eq. (14)] can be written as the vertical integral of a zonally integrated transport as follows (Table 1):

$$\mathrm{AMOC}_{g-\mathrm{sh}} = \int_{-h}^{0} \mathrm{TW}(z)\,dz, \tag{15}$$

with $\mathrm{TW}(z)$ standing for the depth-dependent thermal wind transport ($\mathrm{Sv\,m^{-1}}$) defined from Eq. (14) as

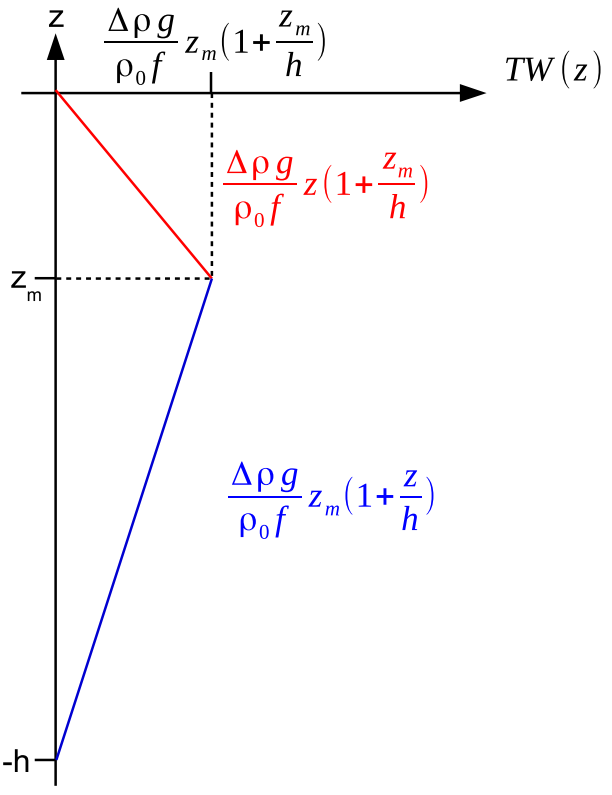

FIG. 1. Depth dependency of the thermal wind transport $\mathrm{TW}(z)$ ($\mathrm{Sv\,m^{-1}}$) for a constant density anomaly $\Delta\rho < 0$. Thermal wind transports are positive (Northern Hemisphere) and increase linearly, from both surface (red) and bottom (blue), to reach a maximum value at the depth z_m of separation between the upper and lower AMOC limbs.

$$\mathrm{TW}(z) = \begin{cases} z\left(1+\dfrac{z_m}{h}\right)\dfrac{g\Delta\rho(z)}{\rho_0 f} & \text{if} \quad z \geq z_m \\ z_m\left(1+\dfrac{z}{h}\right)\dfrac{g\Delta\rho(z)}{\rho_0 f} & \text{if} \quad z < z_m \end{cases}. \tag{16}$$

$\mathrm{TW}(z)$ is the zonally integrated geostrophic AMOC transport (i.e., the transport above the depth z_m) induced by boundary density anomalies $\Delta\rho$ at a particular depth z (see Fig. 1 for its vertical profile). Note that $\mathrm{TW}(z)$ is not the zonally integrated geostrophic transport at a particular depth (although they both have the same units of Sverdrups per meter): it quantifies at all depths a contribution to the upper-limb AMOC transport. It is explicit only in the single-integral AMOC formulation derived above. It directly relates boundary density anomalies at any depth to the AMOC.

We illustrate in Fig. 1 the depth dependency of the thermal wind transport considering a constant density anomaly. For a given density anomaly $\Delta\rho$, the thermal wind transport increases linearly from zero at the surface and bottom to a maximum transport of

$$\mathrm{TW}(z_m) = z_m\left(1+\frac{z_m}{h}\right)\frac{g\Delta\rho}{\rho_0 f} \tag{17}$$

at the depth z_m. For a typical upper-limb depth $z_m = -1000$ m and bathymetry $h = 4000$ m, the thermal wind transport reaches

over two-thirds of its maximum value in the depth range ($-h/2 = -2000$ m; $\frac{2}{3}z_m \simeq -670$ m). Therefore, density anomalies located around the depth of maximum overturning, that is, at the separation between the upper and lower limbs of the AMOC cell, induce most vertically compensated thermal wind transport. In our example and in the observed AMOC at 26.5°N, this depth is closer to the surface than to the bottom—hence, the asymmetry in the vertical dependency of TW(z).

The thermal wind transport and the resulting geostrophic shear AMOC transport also crucially depend on the vertical profile of density anomalies, as discussed and illustrated in section SI3 of the online supplemental material. In addition, the depth z_m largely determines the vertical profile of the thermal wind transport TW(z), as illustrated in Fig. 1. In section SI3, we formulate the dependency of $\mathrm{AMOC}_{g\text{–sh}}$ to the reference depth z_m to show again the key role of the density anomaly profile that determines this depth in the first place.

f. Effect of variable topography

The new AMOC decomposition [Eq. (12)] is exact only in the case of a rectangular zonal basin section. However, the Atlantic Ocean generally has a sloping bathymetry with topographic obstacles such as midoceanic ridges and islands. In section SI4 of the online supplemental material, we formulate an AMOC decomposition that includes the effect of variable topography. The AMOC formulation in the Ekman plus geostrophic approximations is modified in two ways.

In the first modification, the so-called external mode arises from the net contribution of a zonally variable barotropic velocity over variable bathymetry (Hirschi and Marotzke 2007). Indeed, as developed in supplemental section SI4, if a zonal covariance exists between bottom geostrophic velocities and either bathymetry or the upper-limb depth, the following external mode must be added to the $\mathrm{AMOC}_{\mathrm{BTg}}$:

$$\mathrm{AMOC}_{g-\mathrm{EM}} = +\Delta x(0)\left[\frac{\overline{z_m}}{\overline{h}}\overline{h' v_g(-h)'} + \overline{\min(h, -z_m)' v_g(-h)'}\right], \tag{18}$$

where $\Delta x(0) = x_E(0) - x_W(0)$ is the section width at the surface; overbars and primes denote zonal means and anomalies, respectively; $\overline{h}$ is the zonal average bathymetry; $\overline{z_m} = -\overline{\min(h, -z_m)}$ is the zonal average upper-limb depth; $\overline{h' v_g(-h)'}$ is the zonal covariance between bathymetry and bottom geostrophic velocities; and $\overline{\min(h, -z_m)' v_g(-h)'}$ is the zonal covariance between upper-limb depth and bottom geostrophic velocities. As developed in section SI5 of the online supplemental material, $\mathrm{AMOC}_{g\text{–EM}}$ is identical to the overturning transport due to bottom velocities of Baehr et al. (2004) and to the external-mode AMOC transport due to barotropic velocities of Hirschi and Marotzke (2007). As a consequence, it can be interpreted as a projection of the barotropic circulation onto the AMOC. Indeed, if $v_g(-h)$ is larger over shallow than deep bathymetry, the resulting $\mathrm{AMOC}_{g\text{–EM}}$ is positive because a larger fraction of the barotropic geostrophic transport occurs near surface, in the upper AMOC limb. It results from the full zonal section of dynamic sea level and density gradients, which limits the interpretation of the AMOC in terms of the zonally integrated thermal wind. The external mode plays an important role for the full AMOC reconstruction (Baehr et al. 2004) but has a minor contribution to the AMOC low-frequency variability (Hirschi and Marotzke 2007), as will be shown in section 3.

With regard to the second modification, in the presence of topographic obstacles, the thermal wind integration must be performed separately for each subbasin bounded by those obstacles so that both flanks of the obstacles constitute new boundaries. Neglecting them is equivalent to assuming a strictly monotonic topography, and therefore a single zonal boundary, on both sides of the deepest bathymetry h_b. In online supplemental section SI4, we derive both the general $\mathrm{AMOC}_{g\text{–sh}}$ expression with multiple zonal boundaries and its simplified formulation assuming a single western and eastern boundary. In supplemental section SI6, we show with a numerical simulation that results are insensitive to this simplification, so that henceforth we analyze the single boundary $\mathrm{AMOC}_{g\text{–sh}}$ formulation. North of 60°N, the presence of Greenland breaks this hypothesis so that we only analyze the decomposition south of this latitude.

As a consequence, and as developed in supplemental section SI4, the AMOC decomposition under variable but monotonic topography on both sides of the deepest bathymetry h_b is (Table 1)

$$\begin{aligned}\mathrm{AMOC} &= -\left(1 + \frac{\overline{z_m}}{\overline{h}}\right)\frac{\Delta x(0)}{\rho_0 f}\overline{\tau_x} + \frac{g}{\rho_0 f}\left[\int_{-h_b}^{z_m}\left(z_m + \frac{\overline{z_m}}{\overline{h}}z\right)\Delta\rho(z)\,dz + \int_{z_m}^{0} z\left(1 + \frac{\overline{z_m}}{\overline{h}}\right)\Delta\rho(z)\,dz\right] \\ &\quad + \Delta x(0)\left[\frac{\overline{z_m}}{\overline{h}}\overline{h' v_g(-h)'} + \overline{\min(h, -z_m)' v_g(-h)'}\right] \\ &= \mathrm{AMOC}_{E-\mathrm{sh}} + \mathrm{AMOC}_{g-\mathrm{sh}} + \mathrm{AMOC}_{g-\mathrm{EM}},\end{aligned} \tag{19}$$

with $\Delta\rho(z) = \rho[x_E(z), z] - \rho[x_W(z), z]$. The only differences with the rectangular basin case are as follows:

1) The factor z_m/h is replaced by its zonal average $\overline{z_m}/\overline{h}$, which still represents the fraction of the depth-integrated barotropic transport that is located in the upper AMOC limb.
2) Both zonal boundaries vary with depth so that density anomalies must be evaluated at depth-varying boundary locations down to the maximum bathymetry $-h_b$ (see section SI6 of the online supplemental material for a discussion on the boundary definition).
3) An extra term, the external mode, arises as a result of the covariance of bottom geostrophic velocities with either bathymetry or the upper-limb depth (see section SI5 of the online supplemental material for its alternative formulations and supplemental section SI6 for a discussion on

the inclusion of the external mode). Henceforth, we assume bottom velocities to be geostrophic.

Although we focus here on the AMOC defined as the depth maximum of the meridional overturning streamfunction, the above developments are generic to the meridional transport above any depth below the Ekman layer. Therefore, the full overturning streamfunction can be reconstructed from the new AMOC decomposition. Replacing z_m by any depth z in Eq. (19), we obtain a general formulation for the meridional overturning streamfunction:

$$\begin{aligned}\Psi(z) &= -\left(1+\frac{\overline{z}}{\overline{h}}\right)\frac{\Delta x(0)}{\rho_0 f}\overline{\tau_x} + \frac{g}{\rho_0 f}\left[\int_{-h_b}^{z}\left(z+\frac{\overline{z}}{\overline{h}}z'\right)\Delta\rho(z')\,dz' + \int_{z}^{0} z'\left(1+\frac{\overline{z}}{\overline{h}}\right)\Delta\rho(z')\,dz'\right]\\ &\quad + \Delta x(0)\left[\frac{\overline{z}}{\overline{h}}\overline{h' v_g(-h)'} + \overline{\min(h,-z)' v_g(-h)'}\right]\\ &= \Psi_{E-\mathrm{sh}}(z) + \Psi_{g-\mathrm{sh}}(z) + \Psi_{g-\mathrm{EM}}(z),\end{aligned} \tag{20}$$

with again the notation $\overline{z} = -\overline{\min(h,-z)}$ for the zonal average depth of the section above z, and the variable of vertical integration denoted as z'.

g. Contribution of heat, salt, and both boundaries to the geostrophic shear transport

We can separate the geostrophic shear transport into a thermal and haline contribution by decomposing zonal density gradients as follows:

$$\Delta\rho(z) = \rho_0[-\alpha\Delta\Theta(z) + \beta\Delta S_{\mathrm{A}}(z)] \tag{21}$$

where α and β are the nonlinear thermal expansion and haline contraction coefficients, respectively; Θ is the Conservative Temperature, and S_{A} is the Absolute Salinity of seawater. By replacing in Eqs. (14) and (16), we obtain a decomposition of $\mathrm{TW}(z)$ and $\mathrm{AMOC}_{g-\mathrm{sh}}$ (Table 1):

$$\begin{aligned}\mathrm{TW}(z) &= \mathrm{TW}_T(z) + \mathrm{TW}_S(z) \quad \text{and}\\ \mathrm{AMOC}_{g-\mathrm{sh}} &= \mathrm{AMOC}_{gT-\mathrm{sh}} + \mathrm{AMOC}_{gS-\mathrm{sh}},\end{aligned} \tag{22}$$

with the subscripts T and S standing for the thermal and haline contributions.

A similar decomposition can be performed between the western and eastern boundary contributions to the geostrophic shear transport. We simply separate zonally integrated density anomalies into the western and eastern contribution (Table 1):

$$\Delta\rho(z) = -\rho(x_W, z) + \rho(x_E, z). \tag{23}$$

We obtain

$$\begin{aligned}\mathrm{TW}(z) &= \mathrm{TW}_W(z) + \mathrm{TW}_E(z) \quad \text{and}\\ \mathrm{AMOC}_{g-\mathrm{sh}} &= \mathrm{AMOC}_{gW-\mathrm{sh}} + \mathrm{AMOC}_{gE-\mathrm{sh}},\end{aligned} \tag{24}$$

which is only meaningful as an anomaly with respect to a mean state. The subscripts W and E stand for the western and eastern boundary contributions.

3. Dynamical drivers of the centennial AMOC variability in the CNRM-CM6 climate model

a. CNRM-CM6 preindustrial control simulation

The aim of this section is to use a climate model participating in the sixth Climate Model Intercomparison Programme (CMIP6; Eyring et al. 2016) to validate the dynamical AMOC reconstruction that was proposed in section 2 and to interpret its simulated low-frequency AMOC variability. We analyze 1000 years of a preindustrial control simulation of the CNRM-CM6 climate model. This model was recently described and evaluated by Voldoire et al. (2019). It includes the atmospheric model ARPEGE-Climat (Voldoire et al. 2013) coupled via the OASIS coupler (Craig et al. 2017) to the SURFEX land surface model (Decharme et al. 2019), the NEMO, version 3.6, ocean model (Madec and NEMO Team 2016), and the imbedded GELATO sea ice model (Chevallier et al. 2013). Horizontal resolutions are 1.4° over the spectral atmospheric and land surface grid and the nominal 1° resolution over the ocean and sea ice tripolar curvilinear ORCA grid. The atmospheric component has 91 vertical levels, and the ocean component has 75 levels (resolution from 1 m at surface to 200 m at deepest levels). The main ocean physical parameterizations are the turbulent kinetic energy prognostic scheme for vertical turbulence (Blanke and Delecluse 1993), the enhanced vertical diffusion scheme for convection (Madec and NEMO Team 2016), the mesoscale and submesoscale isoneutral mixing (Redi 1982) and eddy-induced velocities (Gent and McWilliams 1990; Fox-Kemper et al. 2008) for tracers, and the tidal mixing parameterization of de Lavergne et al. (2019). In this preindustrial simulation, external forcings (solar, greenhouse gases, and aerosols) are kept constant to their estimated value of year 1850. An 800-yr spinup has been performed prior to the analyzed period and ensures an equilibration of net air–sea heat fluxes at 0.15 W m^{-2}, equivalent to a surface drift of 0.02 K per century. Unless stated otherwise, all model outputs are extracted at the yearly frequency. In what follows, we analyze yearly time series of Atlantic meridional overturning computed offline from the model yearly mean meridional velocities, and its decomposition into an Ekman and geostrophic component deduced from the yearly mean zonal wind stress, Conservative Temperature, and Absolute Salinity at zonal boundaries, and bottom velocities [Eq. (19)].

b. Modeled AMOC and its centennial variability

The model's Atlantic meridional overturning streamfunction Ψ (Fig. 2a) displays an intense clockwise overturning cell down to 3000-m depth, and a weak counterclockwise cell below. The former is the AMOC cell and will be the focus of this work, whereas the latter is associated with the transport

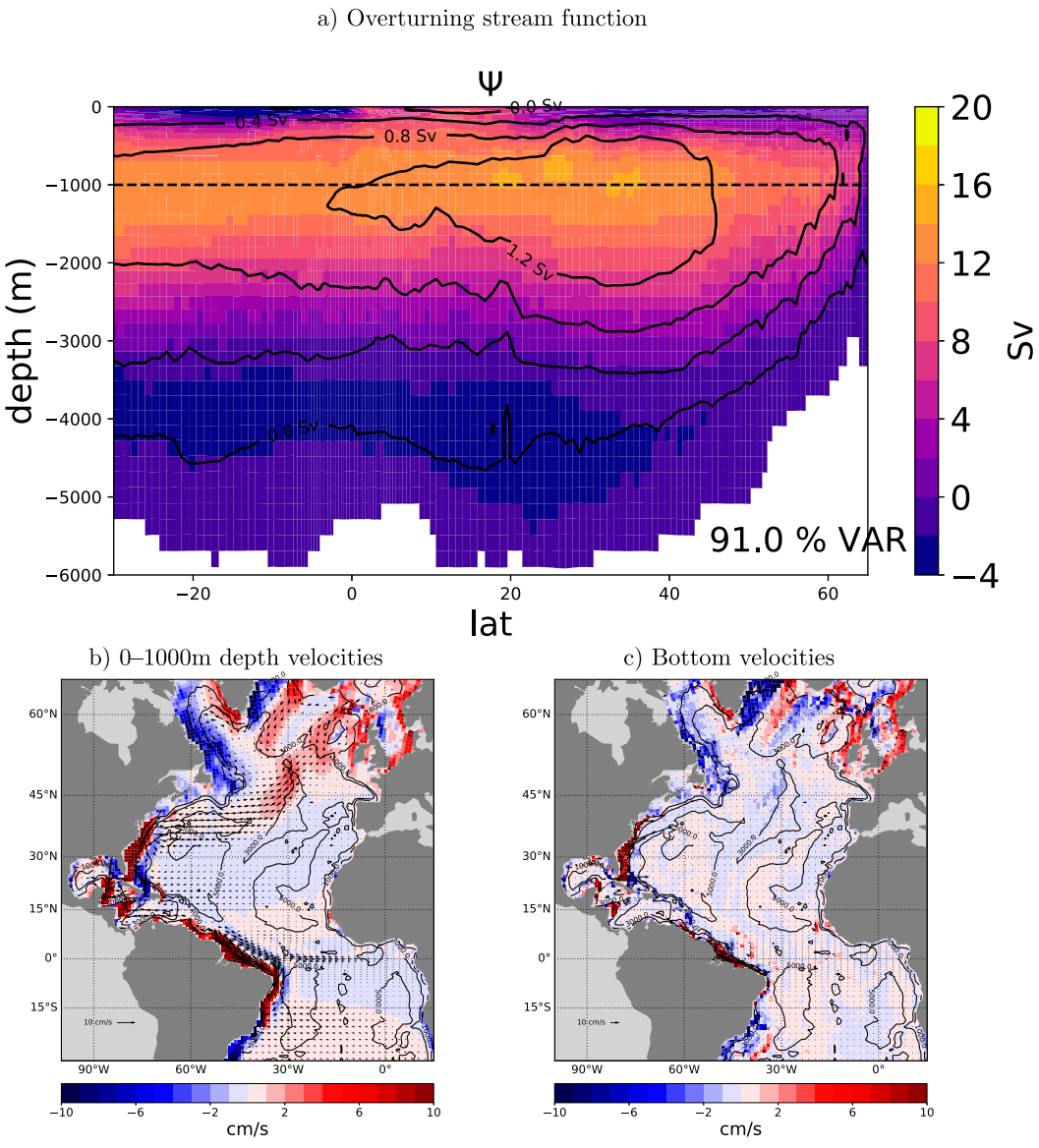

FIG. 2. (a) Mean Atlantic meridional overturning streamfunction Ψ (color shading) and its regression onto the leading multidecadal principal component (contours) in CNRM-CM6. The leading principal component is computed from the 25-yr running average streamfunction and explains 91% of its variance. The horizontal dashed black line shows the depth of maximum overturning. Average currents (vectors) and meridional velocities (shades) over (b) the upper AMOC limb (top 997 m) and (c) at the bottom level in CNRM-CM6. Isobaths are displayed as contours.

and transformation of Antarctic Bottom Water. The AMOC cell reaches a maximum at the model level $z_m = -997$ m on average in the 30°S–60°N latitude range, being relatively constant south of 45°N and then weakening toward high latitudes. z_m has a temporal standard deviation of 22 m, that is, 2% of its long-term average, so that assuming it to be constant is a reasonable approximation. The associated mean meridional currents of its upper limb (above z_m; Fig. 2b) are western intensified at all latitudes except in the subpolar North Atlantic where they are also intense in the interior and eastern boundary. The northward transport occurs predominantly at the western boundary from 15°S to 40°N and in the interior ocean outside those latitudes. Bottom velocities are also intensified along western boundaries and in most of the subpolar North Atlantic (Fig. 2c), illustrating the external-mode contribution to the mean AMOC transport.

The yearly AMOC time series at 30°N (Fig. 3a) reveals an intense low-frequency variability of centennial time scale and of typical peak to peak magnitude ±25% of its long-term average. This centennial cycle is the dominant feature of the 25-yr running average AMOC at all latitudes between 30°S and 60°N. It is very well reproduced by the first principal component of the 25-yr average overturning streamfunction (Fig. 3a),

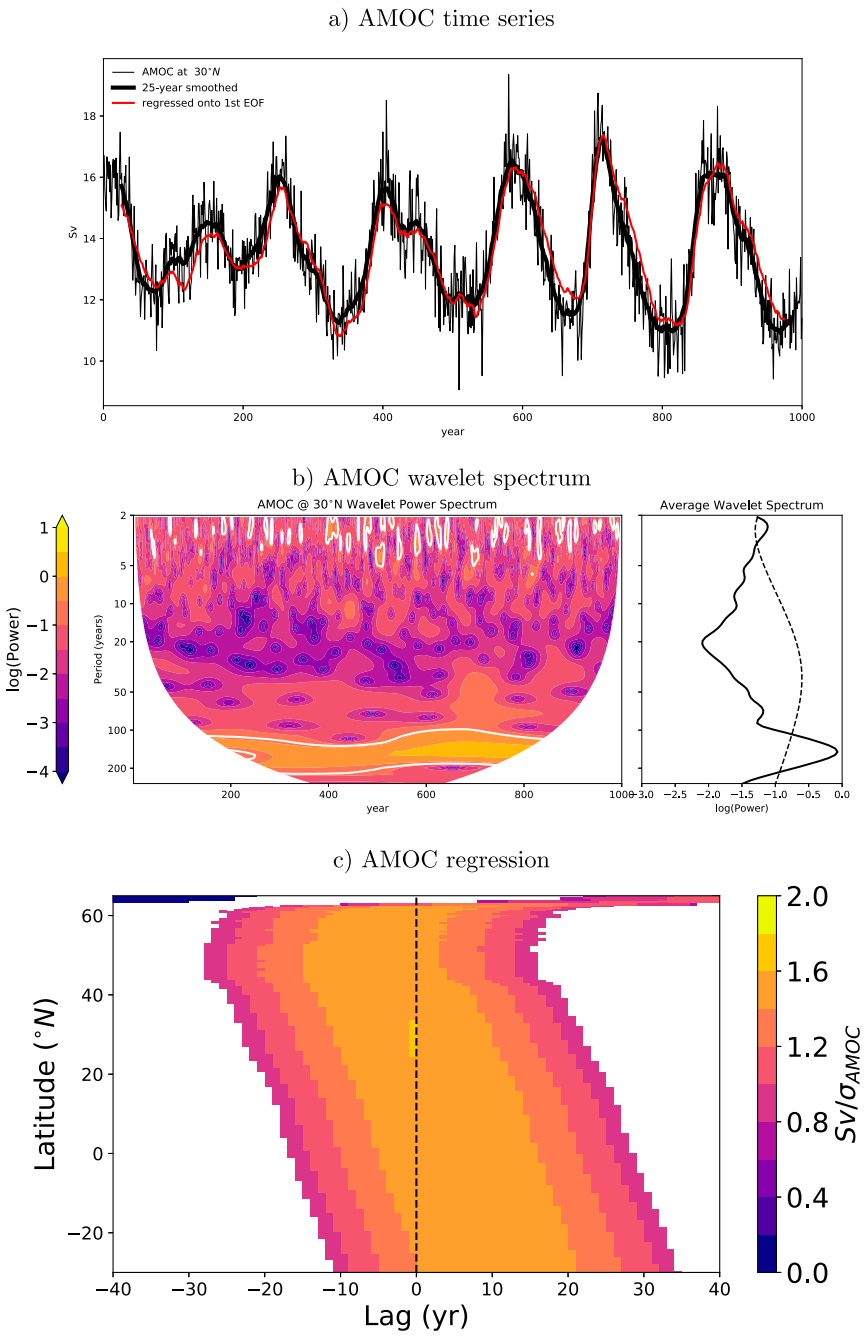

FIG. 3. (a) AMOC time series at 30°N (thin black), its 25-yr running average (thick black) and its regression onto the first principal component of the overturning streamfunction (red) in CNRM-CM6. (b) AMOC at 30°N scale-adjusted wavelet power spectrum (left panel) and its time average (right panel) (Torrence and Compo 1998; Liu et al. 2007). The p value p = 0.05 of an AR1 process is shown by white contour and dashed black line. (c) Lagged regression of the 25-yr average AMOC onto the AMOC at 30°N (p value >0.05 in white; Thomson and Emery 2014).

whose main empirical orthogonal function (EOF) has an interhemispheric structure that resembles the average streamfunction and explains 91% of its variance (Fig. 2a). The scale-adjusted wavelet power spectrum (Fig. 3b; Torrence and Compo 1998; Liu et al. 2007) confirms this significant centennial variability throughout the analysis period, with an energy peak centered at 150 years. Some significant subdecadal variability is also evident, although weaker and more intermittent.

Henceforth, it is removed by only analyzing the 25-yr running average AMOC time series. In what follows, all 25-yr running averages are referred to as multidecadal values.

The regression of the multidecadal AMOC at all latitudes onto its value at 30°N reveals a significant southward propagation of AMOC anomalies from subpolar latitudes (between 45° and 60°N, Fig. 3c). This is consistent with the interhemispheric structure and the large variance explained by the leading EOF of the multidecadal AMOC (Fig. 2a). The maximum lagged regression is reached at 11 years of lag at 30°S, which corresponds to a propagation velocity of $1.9\,\mathrm{cm\,s^{-1}}$, consistent with wave propagation (Johnson and Marshall 2002; Nieves and Spall 2018). We conclude that the AMOC low-frequency variability in CNRM-CM6 is mostly centennial and driven by northern subpolar latitudes. In what follows we will use the decomposition proposed in the previous section to determine how density variations at zonal boundaries drive this cycle.

c. AMOC reconstruction

Following Eq. (19), we reconstruct the sheared Ekman ($\mathrm{AMOC}_{E\text{–sh}}$), geostrophic shear ($\mathrm{AMOC}_{g\text{–sh}}$), and external-mode ($\mathrm{AMOC}_{g\text{–EM}}$) contributions to the AMOC transport from 30°S to 60°N, the sum of which make up the AMOC reconstruction ($\mathrm{AMOC}_E + \mathrm{AMOC}_g$). Figure 4 shows the Hovmöller diagram of the multidecadal AMOC time anomaly, the total reconstruction $\mathrm{AMOC}_E + \mathrm{AMOC}_g$ [Eq. (19)], and its geostrophic shear component $\mathrm{AMOC}_{g\text{–sh}}$ [Eq. (14)]. Note that, as mentioned in the previous section, the deep tropics (within 2° of the equator) are excluded from the analysis because the dynamics cannot be assumed to be quasigeostrophic there. The meridionally coherent centennial AMOC anomalies are the dominant feature. They are reasonably well reproduced by the total AMOC reconstruction, both in terms of timing and magnitude. The magnitude of variability is locally overestimated in the Tropical and Subtropical North Atlantic. This feature was also evident in previous AMOC reconstructions (e.g., Hirschi and Marotzke 2007). In the 10°–20°N latitude band, errors are related to $\mathrm{AMOC}_{g\text{–sh}}$ (Fig. 4c). They are mostly due to the neglect of topographic obstacles such as the Antilles archipelago, as shown in the sensitivity study on the boundary definition (section SI6 of the online supplemental material). In the 20°–30°N latitude band, errors are dominated by $\mathrm{AMOC}_{g\text{–EM}}$ (not shown). They are likely related to the assumption of geostrophic bottom velocities and to approximations related to the model's Arakawa C grid. Most significantly, the geostrophic shear component alone is able to reproduce most of this centennial AMOC variability. This indicates that the low-frequency AMOC variability of CNRM-CM6 can largely be explained by the zonally integrated thermal wind balance, itself by definition solely determined by density anomalies at the zonal boundaries of the Atlantic Ocean. Results are mostly unchanged when using an $\mathrm{AMOC}_{g\text{–sh}}$ formulation with multiple zonal boundaries (see supplemental section SI6), which confirms the dominant role of westernmost and easternmost densities in driving the AMOC variability in CNRM-CM6.

For a more quantitative assessment of the AMOC reconstruction, we turn to the Taylor diagram of all terms of the reconstruction as a function of the total multidecadal AMOC (Fig. 5a; Taylor 2001). It displays in a single diagram the temporal correlation r, the normalized standard deviation σ_n, and the normalized root mean square errors (RMSE_n) of every component with respect to the total AMOC averaged over latitude bands (colored symbols) and its full meridional average over the 30°S–60°N latitude band excluding the deep tropics (black symbols). The σ_n and RMSE_n are defined at a given latitude band as

$$\sigma_n = \sigma/\sigma_{\mathrm{tot}} \quad \text{and} \tag{25}$$

$$\mathrm{RMSE}_n = \mathrm{RMSE}/\sigma_{\mathrm{tot}}, \tag{26}$$

with σ_{tot} being the temporal standard deviation of the total AMOC and σ and RMSE being the temporal standard deviation and root-mean-square error, respectively, of each term of the AMOC decomposition with respect to the total AMOC. The sheared Ekman component $\mathrm{AMOC}_{E\text{–sh}}$ has almost no low-frequency variability, with $\sigma_n < 0.1$ at all latitudes, meaning that its variability is over one order of magnitude lower than the total AMOC. In addition, it has weak to negative correlations to the AMOC, with $r < 0.3$ at all latitude ranges. Therefore, it does not contribute to the AMOC low-frequency variability. By contrast, the geostrophic shear transport $\mathrm{AMOC}_{g\text{–sh}}$ largely dominates the total AMOC variability. Indeed, its temporal correlation is $r > 0.9$ at all latitudes, meaning that it explains over 80% of the total AMOC variance. Its variability compares well to that of the total AMOC, with σ_n falling within 30% of unity. As a consequence, its RMSE is below half the multidecadal AMOC standard deviation ($\mathrm{RMSE}_n < 0.5$). The external-mode transport $\mathrm{AMOC}_{g\text{–EM}}$ generally correlates positively with the total AMOC, with $-0.2 < r < 0.8$, but its normalized standard deviation is $\sigma_n < 0.2$ at all latitudes. This means that its contribution to the AMOC low-frequency variability of CNRM-CM6 is minor. The total AMOC reconstruction $\mathrm{AMOC}_E + \mathrm{AMOC}_g$ largely resembles the geostrophic shear component, with some marginal improvement related to the inclusion of the external mode. It also explains over 80% of the AMOC variance at all latitudes and its RMSE_n is reduced on average. The meridional mean AMOC reconstruction summarizes well the main results, with even better scores than individual latitudinal bands: the reconstruction proposed in Eq. (19) is excellent at reproducing the low-frequency AMOC variability of CNRM-CM6, which is overwhelmingly driven by the geostrophic shear component.

d. Drivers of the thermal wind AMOC variability

We have previously diagnosed that most of the multidecadal AMOC variability is driven in CNRM-CM6 by its geostrophic shear component, itself entirely determined by densities at both zonal boundaries. Figure 6 displays the hydrographic signature at superficial (0–500 m) and intermediate (500–1500 m) depths of this variability as the hydrographic regression onto the multidecadal geostrophic shear transport $\mathrm{AMOC}_{g\text{–sh}}$ (results are almost identical when regressed onto the total AMOC). At each location, the layer-averaged hydrography is regressed onto the multidecadal geostrophic shear $\mathrm{AMOC}_{g\text{–sh}}$ transport time series at the same latitude, in

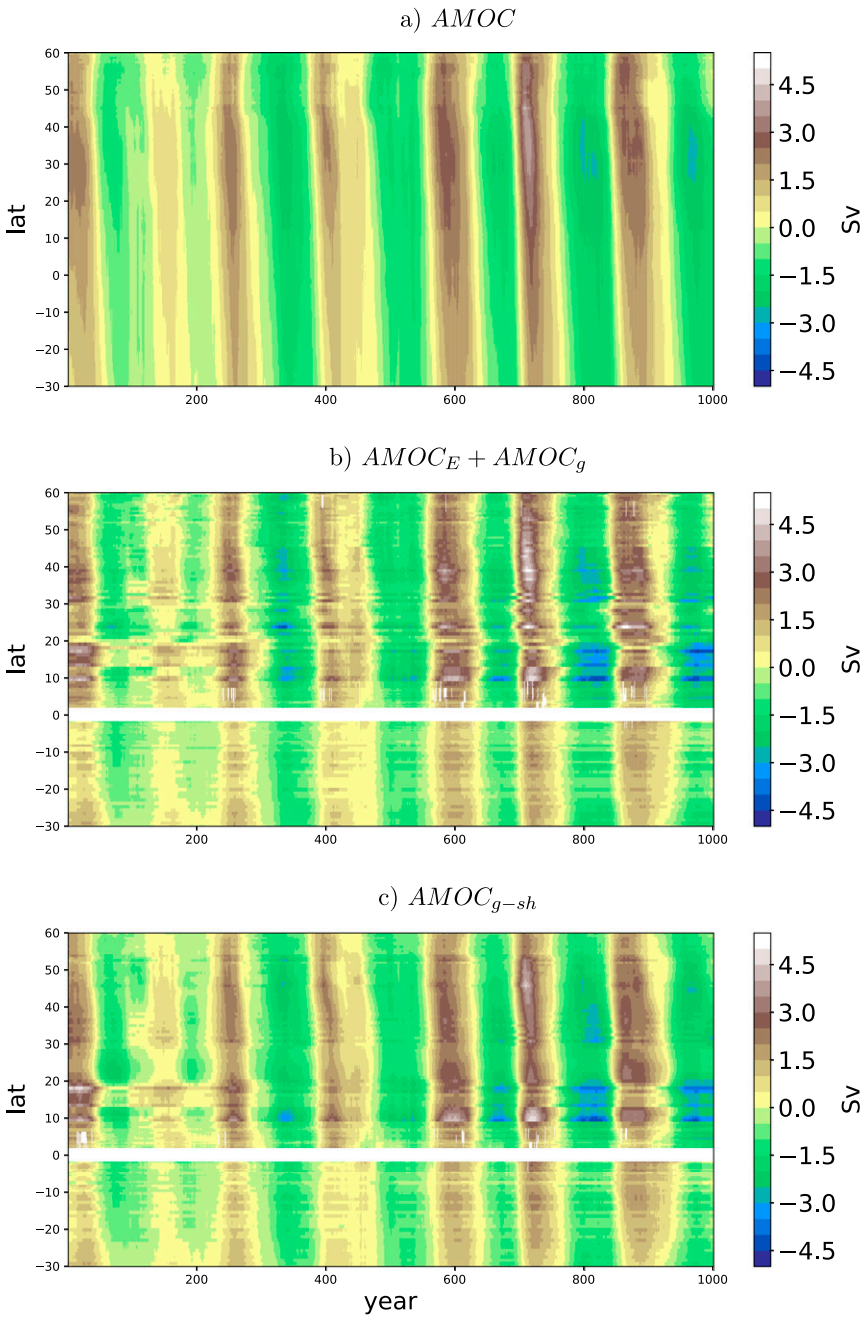

FIG. 4. (a) Hovmöller diagrams of the 25-yr running average (a) AMOC time anomaly, (b) total Ekman plus geostrophic AMOC reconstruction ($AMOC_E$ + $AMOC_g$), and (c) its geostrophic shear component ($AMOC_{g-sh}$) as a function of latitude in CNRM-CM6.

agreement with the diagnostic nature of the thermal wind relation. We first analyze the density anomaly associated with the $AMOC_{g-sh}$ variability (Figs. 6a,b). Potential density at the reference pressure 1000 dbar (σ_1) is displayed because it gives very similar results to in situ density and allows us to compare the average densities at different depths (contours in Figs. 6a,b). At superficial depths, the $AMOC_{g-sh}$ variability is associated with a dense anomaly along the western boundary of the North Atlantic and the eastern boundary of the South Atlantic. At the opposite boundary, the density anomaly is generally weaker, with the exception of the 15°S–5°N latitude range where anomalies are zonally coherent. This is consistent with a northward geostrophic AMOC transport associated with a westward density gradient in the North Atlantic and an eastward density gradient in the South Atlantic, in agreement with the changing sign of the Coriolis parameter across the

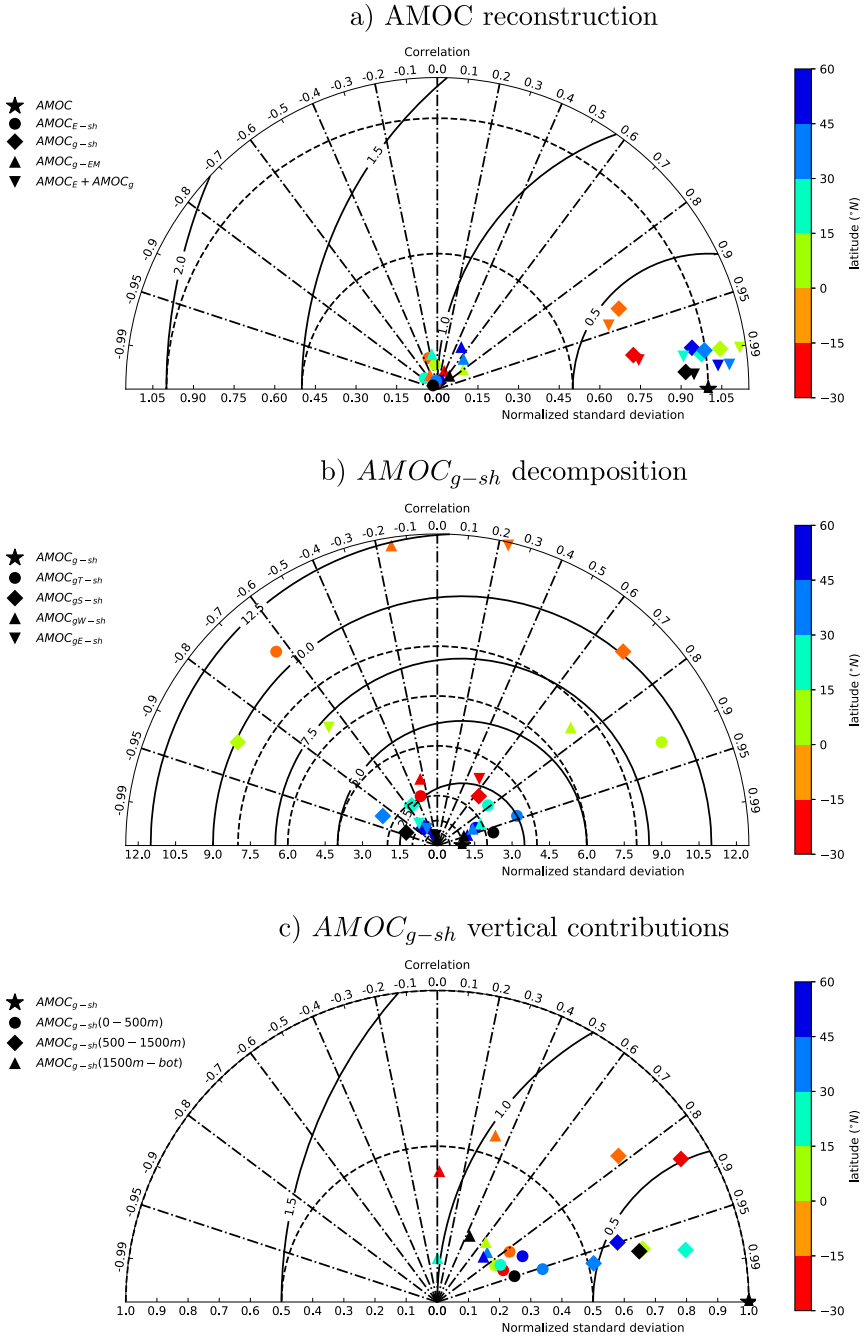

FIG. 5. Taylor diagrams of the 25-yr average (a) Ekman shear ($AMOC_{E–sh}$; circles), geostrophic shear ($AMOC_{g–sh}$; diamonds), external mode ($AMOC_{g–EM}$; downward triangles), and total Ekman plus geostrophic transports ($AMOC_E + AMOC_g$; triangles) as a function of the total AMOC at the same latitude (star); (b) thermal ($AMOC_{gT–sh}$), haline ($AMOC_{gS–sh}$), western ($AMOC_{gW–sh}$), and eastern ($AMOC_{gE–sh}$) boundary contributions to $AMOC_{g–sh}$ as a function of $AMOC_{g–sh}$; and (c) upper [$AMOC_{g–sh}$(0–500 m)], middepth [$AMOC_{g–sh}$(500–1500 m)], and deep [$AMOC_{g–sh}$(1500 m–bottom)] layer contributions to $AMOC_{g–sh}$ as a function of $AMOC_{g–sh}$. Colors indicate the latitude (15° average), with black symbols indicating the full meridional mean.

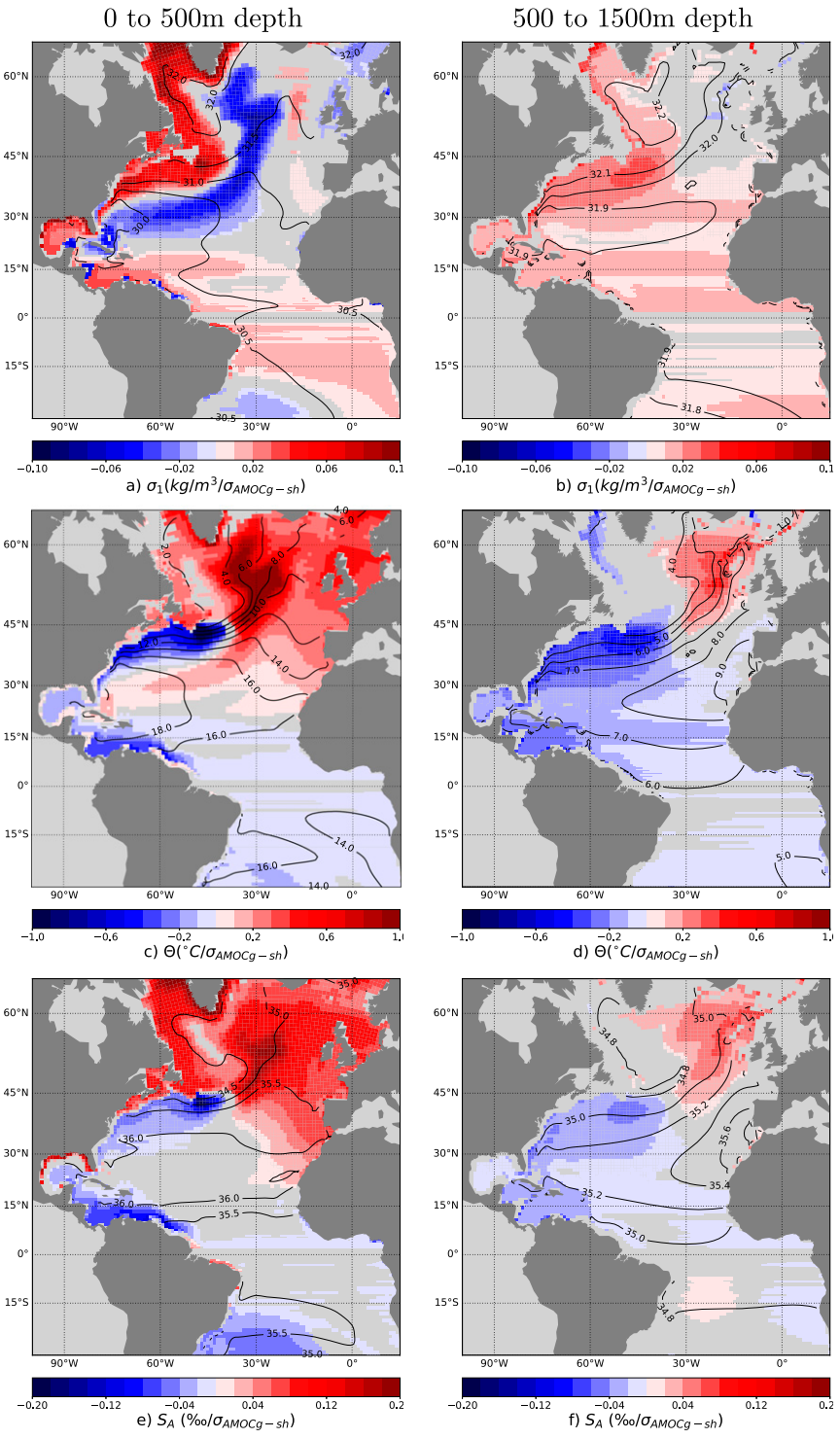

FIG. 6. Regression of the multidecadal (a),(b) potential density σ_1; (c),(d) Conservative Temperature Θ; and (e),(f) Absolute Salinity S_A in the (left) 0–500-m and (right) 500–1500-m depth layers onto the multidecadal geostrophic shear AMOC transport. Units are per standard deviation of $AMOC_{g-sh}$ ($\sigma_{AMOCg-sh}$). Regions with a p value $p > 0.05$ (Thomson and Emery 2014) are in gray, and contours represent the average hydrography.

equator. Also, the reversal of boundary across the equator is consistent with the AMOC anomaly propagation to the South Atlantic. At intermediate depths, the density anomaly occurs predominantly at the western boundary north of 35°N. Southward, density anomalies show a zonal coherence and therefore some compensation between both boundaries. At both depth ranges, the subpolar density regresses positively with the multidecadal AMOC over most of the Labrador Sea, particularly in the vicinity of its boundaries. This feature was found to be common among the CMIP5 ensemble (Roberts et al. 2013; Ortega et al. 2017). Below 1500-m depth, regressed density anomalies are mostly insignificant at both boundaries ($p > 0.05$; not shown). Note that, although they are visible away from boundaries at superficial depths (Fig. 6a), large density anomalies have no direct influence on the $\mathrm{AMOC}_{g\text{–sh}}$ transport, which is exclusively a function of densities at the zonal boundaries [see Eq. (19)].

We now decompose the geostrophic shear transport into its thermal, haline, western and eastern boundary contributions, following Eqs. (22) and (24). We first turn to the thermal and haline contributions to the $\mathrm{AMOC}_{g\text{–sh}}$ variability (Fig. 5b). The large spread in the Taylor diagram indicates that there are strong density compensations in zonally integrated thermal and haline anomalies throughout the Atlantic Ocean. Indeed, the thermally driven transport $\mathrm{AMOC}_{gT\text{–sh}}$ and its haline-driven counterpart $\mathrm{AMOC}_{gS\text{–sh}}$ have large variabilities of $1 < \sigma_n < 11$. As a result, the mean error is large, with $\mathrm{RMSE}_n > 0.5$ in all cases. They have almost symmetric locations with respect to the $r = 0$ axis, meaning that they are strongly anticorrelated and compensated. Another striking feature is the contrasting behavior between the northern and Southern Hemisphere. Throughout the North Atlantic, the geostrophic shear transport is thermally driven, with correlations of $0.7 < r < 0.95$ for the thermal transport as opposed to $r < -0.3$ for the haline transport. This means that temperature variations explain between 50% and 85% of the geostrophic shear transport variance in the North Atlantic. Conversely, in the South Atlantic, the salinity contribution drives the AMOC variability, with $0.65 < r < 0.7$, whereas the thermal contribution opposes it with $r < -0.3$. Note that in this case, salinity variations only explain 35%–40% of the geostrophic shear transport variance. Therefore, in both hemispheres, because of large density-compensating thermohaline variations, a large fraction of the AMOC variance cannot be explained by individual contributions. This limitation in the understanding of the sources of AMOC variability is inherent to the equation of state of seawater. Overall, the meridional mean AMOC variability is largely dominated by temperature variations, reflecting the dominance of the North Atlantic in driving the centennial AMOC cycle of the CNRM-CM6 model.

The maps of regressed temperature (Figs. 6c,d) and salinity (Figs. 6e,f) anomalies onto the multidecadal $\mathrm{AMOC}_{g\text{–sh}}$ transport illustrate the associated patterns of variability at both boundaries. Temperature and salinity anomalies generally largely correlate, with a warm and salty signal at subpolar latitudes when the AMOC is strong but a cold and fresh signal further southward. The signal differs between superficial and intermediate depths, especially in the western subpolar gyre. In the superficial layer (Figs. 6c,e), the dense western anomaly is salinity driven north of 45°N but temperature driven south of it. By contrast, at intermediate depths (Figs. 6d,f), this anomaly is temperature driven throughout the western boundary of the North Atlantic. Overall, the AMOC transport variability is temperature driven in the North Atlantic (Fig. 5b), which means that the intermediate depth temperature anomalies are the main driver of the geostrophic shear $\mathrm{AMOC}_{g\text{–sh}}$ transport. This is consistent with theoretical predictions that density anomalies around the depth of separation between upper and lower limbs are most efficient at driving AMOC transport variations. Muir and Fedorov (2017) also found a predominant effect of temperature anomalies on density anomalies associated with the multidecadal AMOC variability found in over half of the CMIP5 models. However, they diagnosed it in the superficial layer whose density variations are salinity driven north of 45°N in CNRM-CM6 (Fig. 6e). Therefore, the hydrographic signature of the centennial variability in CNRM-CM6 differs from the multidecadal mode identified by Muir and Fedorov (2017) in the CMIP5 ensemble. Although significant thermohaline anomalies are visible at the eastern subpolar region, they have opposite effects on density, being either warm and salty for strong AMOC or cold and fresh for weak AMOC. As a result of this thermohaline density compensation, density anomalies at the eastern subpolar region are weak. Finally, no clear picture is evident in the South Atlantic. This is consistent with the small fraction of AMOC variance explained by individual contributions because of large density compensations.

Analysis of the respective contributions of the western and eastern boundaries to the geostrophic shear transport gives similar results to the thermohaline decomposition (Fig. 5b): large compensating density variations at both boundaries and a contrasting behavior between both hemispheres. Again, this hemispheric asymmetry is in agreement with the patterns of regressed density anomalies of Figs. 6a and 6b. It is consistent with a meridionally coherent AMOC variability. The large spread in variabilities with $0.3 < \sigma_n < 13$ and the relative symmetry of western and eastern boundary contributions about the $r = 0$ axis are indicative of large and compensating contributions at each boundary. As a consequence, errors can reach large values of up to $\mathrm{RMSE}_n \simeq 12$. However, the picture is clearer in the North Atlantic Ocean, which is largely dominated by the western boundary. Indeed, it has correlations of $r > 0.7$ with the total geostrophic shear transport, which is even more true for the subpolar North Atlantic (in the 45°–60°N latitude range) where $r = 0.96$. This means that the western boundary explains over 50% of the total geostrophic shear transport variance in the North Atlantic, and even over 90% of it at subpolar latitudes. On the contrary, the eastern boundary contribution is weakly anticorrelated to the total transport, with $r < -0.2$. Conversely, the South Atlantic is dominated by eastern boundary density variations, although with poor correlations of $0.2 < r < 0.55$. In that hemisphere, density variations at both boundaries are mostly compensated, so that the total geostrophic shear transport is a small residual. Because of this compensation, only 5%–30% of its variance is explained by the eastern boundary. Overall, the meridional mean AMOC

variability is largely dominated by western boundary variations, reflecting again the dominance of the North Atlantic in driving the centennial AMOC variability.

e. Thermal wind transport as a function of depth

We turn to the layer-integrated thermal wind transport (in Sverdrups). We integrate vertically Eq. (16) over the near-surface layer (0–500-m depth), the intermediate layer (500–1500-m depth), and the deep layer (below 1500-m depth) to determine which vertical layers drive the low-frequency AMOC variability in CNRM-CM6. Figure 5c shows the Taylor diagram of the integrated thermal wind transport over those layers as a function of the geostrophic shear transport $\mathrm{AMOC}_{g-\mathrm{sh}}$, which makes up the sum of all three contributions. Overall, the intermediate layer largely dominates the $\mathrm{AMOC}_{g-\mathrm{sh}}$ variability, with temporal correlations of $r > 0.75$ and normalized standard deviations of $\sigma_n > 0.5$ at all latitude bands. The surface layer also largely correlates to the total geostrophic shear transport, with $r > 0.8$. However, it has a weak variability with $\sigma_n < 0.4$ at all latitudes. This result has important methodological consequences: boundary densities of the surface and intermediate layers covary with the total AMOC, so that a classical statistical analysis (either correlation or regression coefficients) would suggest that they both drive the AMOC variability. However, our physical decomposition reveals that the surface contribution is minor and despite large correlations, the surface layer induces little thermal wind AMOC variability. The deep layer correlates poorly with the total geostrophic shear transport south of 30°N, with $r < 0.4$. Northward, it has larger correlations of $0.6 < r < 0.8$, but it induces little transport variability with $\sigma_n < 0.3$. Therefore, the deep layers play a minor role in driving the AMOC variability, although at northern subpolar latitudes, significant correlations can be found between deep densities at zonal boundaries and the AMOC. This is consistent with density anomalies propagating to depth (e.g., through deep convection and overflows) but being too weak at depth to drive the AMOC variability.

We now regress the thermal wind transport $\mathrm{TW}(z)$ ($\mathrm{Sv\,m^{-1}}$) as a function of depth and latitude onto the multidecadal $\mathrm{AMOC}_{g-\mathrm{sh}}$ transport at each latitude to investigate further the vertical levels that drive the low-frequency AMOC variability in CNRM-CM6 (Fig. 7a). We recall that $\mathrm{TW}(z)$ depends exclusively on density anomalies at both zonal boundaries and that its vertical integral is the geostrophic shear transport $\mathrm{AMOC}_{g-\mathrm{sh}}$ [Eqs. (15) and (16)]. Consistent with the theoretical predictions from section 2, the thermal wind transport has a maximum regression at intermediate depths, in the 200–1500-m depth range (Fig. 7a). Near the surface, $\mathrm{TW}(z)$ is generally weak. Below 1500-m depth, the thermal wind transport variability is weak, apart from localized areas around 4000–5000-m depth in the tropical North Atlantic. This indicates that zonal density gradients vary too little below that depth to drive AMOC variations. The density regression onto the multidecadal $\mathrm{AMOC}_{g-\mathrm{sh}}$ transport (Fig. 7b) generally shows a larger signal near surface and weaker anomalies at intermediate depths. Despite most density variations occurring above 500-m depth, they induce a weak thermal wind transport because by definition, they only affect velocities in the uppermost fraction of the water column [see the interpretation of Eqs. (8) and (16)]. Conversely, strongest thermal wind transports are induced by weaker density variations that occur at intermediate depths. Therefore, the new AMOC decomposition established in section 2 gives a theoretical insight into why density anomalies alone are a poor predictor of the AMOC variability.

We finally regress the thermal, haline, western, and eastern boundary contributions to the thermal wind transport at each latitude and depth onto the multidecadal $\mathrm{AMOC}_{g-\mathrm{sh}}$ transport at the same latitude (Figs. 7c–f). The regressions of the thermal and haline thermal wind transport onto the multidecadal variability of $\mathrm{AMOC}_{g-\mathrm{sh}}$ (Figs. 7c,d) largely exceed that of the total $\mathrm{TW}(z)$ (Fig. 7a). This indicates a large density compensation. The thermal and haline transport regressions are systematically of opposite sign, meaning that density variations have either a cold and fresh, or a warm and salty signature. In the North Atlantic, the thermal component dominates whereas the haline transport opposes the total thermal wind transport. This feature, and the depths of maximum transport, are consistent with the intermediate-depth and temperature-driven $\mathrm{AMOC}_{g-\mathrm{sh}}$ variability over the North Atlantic. Throughout the tropical and South Atlantic, south of 10°N, large regressions are found for both the thermal and haline contributions in the 1500–3500-m depth range (Figs. 7c,d), with almost no signature in the total thermal wind transport and density (Figs. 7a,b). This deep thermohaline variability at almost constant density explains the poor correlation and the large normalized standard deviation of the thermal and haline contributions to the $\mathrm{AMOC}_{g-\mathrm{sh}}$ transport (Fig. 5b). It also explains how the South Atlantic AMOC variability is to a limited extent salinity driven in a vertically integrated sense (Fig. 5b), although at the intermediate depths that drive the $\mathrm{AMOC}_{g-\mathrm{sh}}$ (Figs. 5c and 7a), the transport variability is temperature driven (Figs. 7c,d).

Similar to the thermal and haline contributions, the eastern and western boundary thermal wind transports have large and mostly compensating contributions to the $\mathrm{AMOC}_{g-\mathrm{sh}}$ south of 35°N (Figs. 7e,f). It means that density anomalies generally covary at both zonal boundaries. North of 35°N, the western boundary largely dominates at all depths, hence explaining its dominance in the total $\mathrm{AMOC}_{g-\mathrm{sh}}$ (Fig. 5b). By contrast, the eastern boundary only has a localized negative contribution in the 1000–1200-m depth range—hence its weak role in the total $\mathrm{AMOC}_{g-\mathrm{sh}}$ variability north of 30°N (Fig. 5b). Again, we see the North Atlantic dominated by the western boundary and the South Atlantic dominated by the eastern boundary, in agreement with previous results on the $\mathrm{AMOC}_{g-\mathrm{sh}}$ variability (Fig. 5b). In the deep tropical Atlantic (below 4000-m depth and 10°S–20°N latitude range), both boundaries exhibit locally large variabilities, but they almost entirely compensate and therefore marginally contribute to the total transport. We conclude on the dominant role of the 500–1500-m depth layer in driving the low-frequency AMOC variability of CNRM-CM6 model. The thermohaline and zonal boundary decomposition shows again large density compensations, particularly in the South Atlantic.

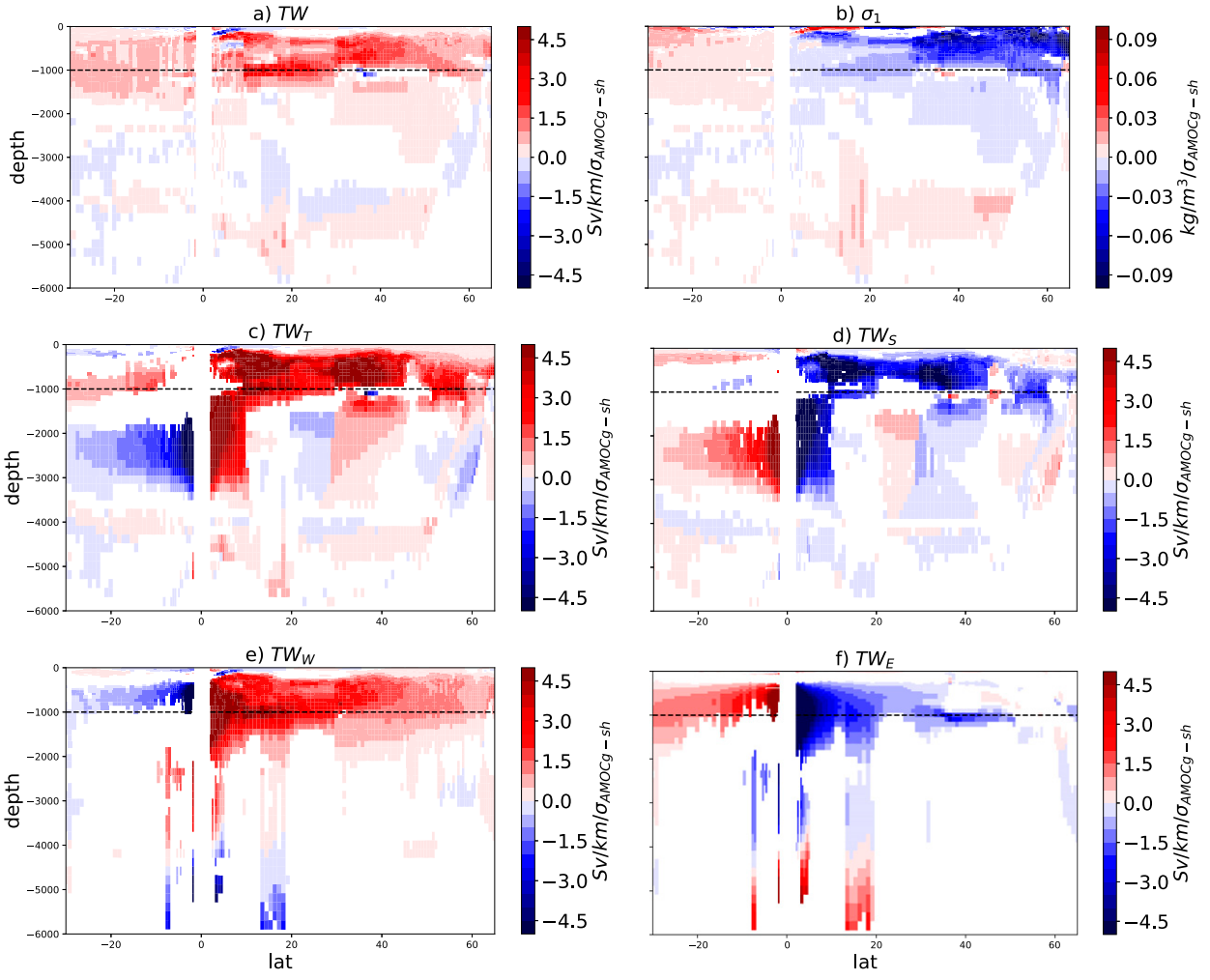

FIG. 7. (a) Regression of the multidecadal thermal wind transport TW onto the multidecadal geostrophic shear $AMOC_{g-sh}$ transport [Sv km^{-1} ($=1000\,m^2\,s^{-1}$) per $AMOC_{g-sh}$ standard deviation ($\sigma_{AMOCg-sh}$)]. (b) As in (a), but for the multidecadal density anomaly $\Delta\rho = \rho(x_E) - \rho(x_W)$ (kg m^{-3} per $\sigma_{AMOCg-sh}$). As in (a), but for the multidecadal (c) thermal (TW_T), (d) haline (TW_S), (e) western (TW_W), and (f) eastern (TW_E) boundary contributions to the total thermal wind transport TW (Sv km^{-1} per $\sigma_{AMOCg-sh}$). Regions with a p value $p > 0.05$ (Thomson and Emery 2014) are in white. The horizontal dashed black line shows the depth of maximum overturning.

4. Sources of dense water variability in CNRM-CM6

a. Deep convection

The new dynamical AMOC decomposition has revealed that the centennial AMOC variability of CNRM-CM6 is driven by the thermal wind transport caused by density (mostly temperature) anomalies at intermediate depths of the subpolar North Atlantic western boundary, namely, the western boundary of the Labrador Sea. We investigate here the link with the two predominant mechanisms of dense water formation in that region: deep convection and dense water overflows (Buckley and Marshall 2016). Figure 8a shows the climatology of the annual maximum mixed layer depth (MLD) in the subpolar North Atlantic. As documented by Voldoire et al. (2019) and Séférian et al. (2019), the GIN Seas experience intense deep convection, whereas it is more limited in extent and depth in the Labrador Sea and in the Scotland Sea. In the GIN Seas and Labrador Sea, the regression of the MLD anomaly onto the first multidecadal AMOC principal component (PC1, Fig. 8b) shows large anomalies. They are positive and strongest (above 200 m anomaly) around zero lag with a maximum when MLDs lead the AMOC by 9 years. They reach minima at a lead time of 88 years and a lag time of 64 years, which corresponds approximately to 10 years prior to the half phase of the centennial AMOC cycle documented in section 3. This means that enhanced (reduced) high-latitude deep convection precedes the AMOC maximum (minimum) by typically 10 years. The regression of MLDs in the Scotland Sea convection area is weaker by an order of magnitude, with significant positive anomalies within 20 years of lead–lag time of the AMOC PC1. The contours of the 9-yr lead time MLD regression onto the AMOC PC1 (Fig. 8a) show a large area with regressed anomalies up to 850 m within the GIN Seas, and a more localized area with anomalies above 250 m along

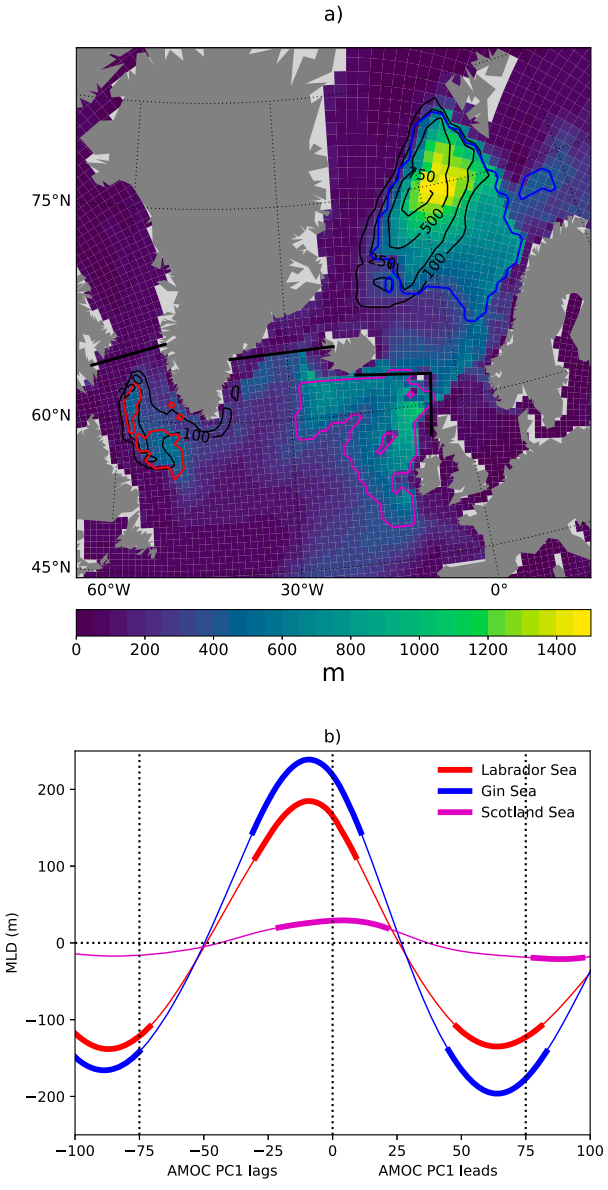

FIG. 8. (a) Annual maximum MLD (computed from monthly means) in the CNRM-CM6 PiControl run (shades), and its 9-yr lead regression onto the multidecadal AMOC PC1 (black contours). Convection areas with MLD > 400 m are within the red, blue, and magenta contours in the Labrador, Greenland–Iceland–Norwegian (GIN), and Scotland Seas, respectively. Black lines locate the Davis and Denmark Straits, and the Iceland–Faroe and Faroe–Scotland channels. (b) Lead–lag regression of the annual maximum MLD at the convection sites of the Labrador, GIN, and Scotland Seas onto the AMOC PC1. Thick and thin line sections indicate that $p < 0.05$ and $p > 0.05$, respectively (Thomson and Emery 2014).

the western boundary of the Labrador Sea. Therefore, the GIN Seas deep convection can be a driver of the AMOC low-frequency variability provided the dense water signal propagates through the GIN Seas overflows to the middepths of the western Labrador Sea. By contrast, Labrador Sea deep convection variability occurs along its western boundary: it is therefore a direct driver of the centennial AMOC variability in CNRM-CM6. The role of Labrador Sea deep convection in the AMOC low-frequency variability is common among climate models and it has already been documented by numerous studies (e.g., Jungclaus et al. 2005; Dong and Sutton 2005; Danabasoglu 2008; Ortega et al. 2012; Lohmann et al. 2014; Ruprich-Robert and Cassou 2015).

We diagnose in Fig. 9 the hydrographic profile regression onto the AMOC PC1 in the GIN Seas and the Labrador Sea convection areas, when water mass properties lead the AMOC by 9 years. In both regions, a significant densification occurs above 1400-m depth, which is intensified over the top 500-m depth (Fig. 9c). The top 250-m depth is anomalously warm (Fig. 9a) whereas the top 500 m is anomalously salty (Fig. 9b), making the top 500-m density anomaly salinity driven (Fig. 9c). Below 500-m depth, the behavior differs between both basins: in the Labrador Sea, we find the cold anomaly in the 500–1500-m depth range that dominates the density signal at those depths (Fig. 9c) and drives, as was shown in section 3, the AMOC transport variability in CNRM-CM6. In the GIN Seas, the middepth density anomaly is salinity driven with a warm temperature signal. Below 1500-m depth, hydrographic regressions become insignificant with the exception of a density-compensating warm and saline signal in the GIN Seas. Therefore, Labrador Sea deep convection produces dense water properties that are consistent with the middepth driver of the AMOC found in section 3. Again, the link with GIN Seas convection is not clear. In addition, the surface-intensified density anomaly indicates that in both regions, deep convection variability is salinity driven. This finding is also common to numerous studies of the AMOC low-frequency variability in climate models (Vellinga and Wu 2004; Dong and Sutton 2005; Jungclaus et al. 2005; Msadek and Frankignoul 2009; Jackson and Vellinga 2013; Ruprich-Robert and Cassou 2015). The warm and salty anomaly in the surface ocean can seem at odds with the cold anomaly found at middepths in the Labrador Sea. However, such an anomaly can be understood when considering the average (climatological) stratification in the region: the top 500 m are colder and fresher than the waters between 500 and 1500-m depth (contours in Figs. 6c,e). The temperature anomaly reduces but does not cancel this vertical inversion: 9 years prior to the AMOC maximum, the upper 500 m in the Labrador Sea remain colder than the waters below. Hence the cold signal at middepth associated to a deeper mixed layer in the Labrador Sea.

b. *Overflows*

Figure 10 shows the 9-yr lead regression of velocities and densities across all high-latitude straits of the subpolar gyre onto the AMOC PC1 (results are insensitive within a 10-yr lead–lag time window). At the Davis Strait (Figs. 10a,b), the dominant features are: the southward advection of light waters above 300 m almost across the section, and a dense water overflow toward the Labrador Sea below 500-m depth. The regression onto the AMOC PC1 is characterized by a densification throughout the section. Southward velocities of the surface flow and the overflow are both intensified. Most

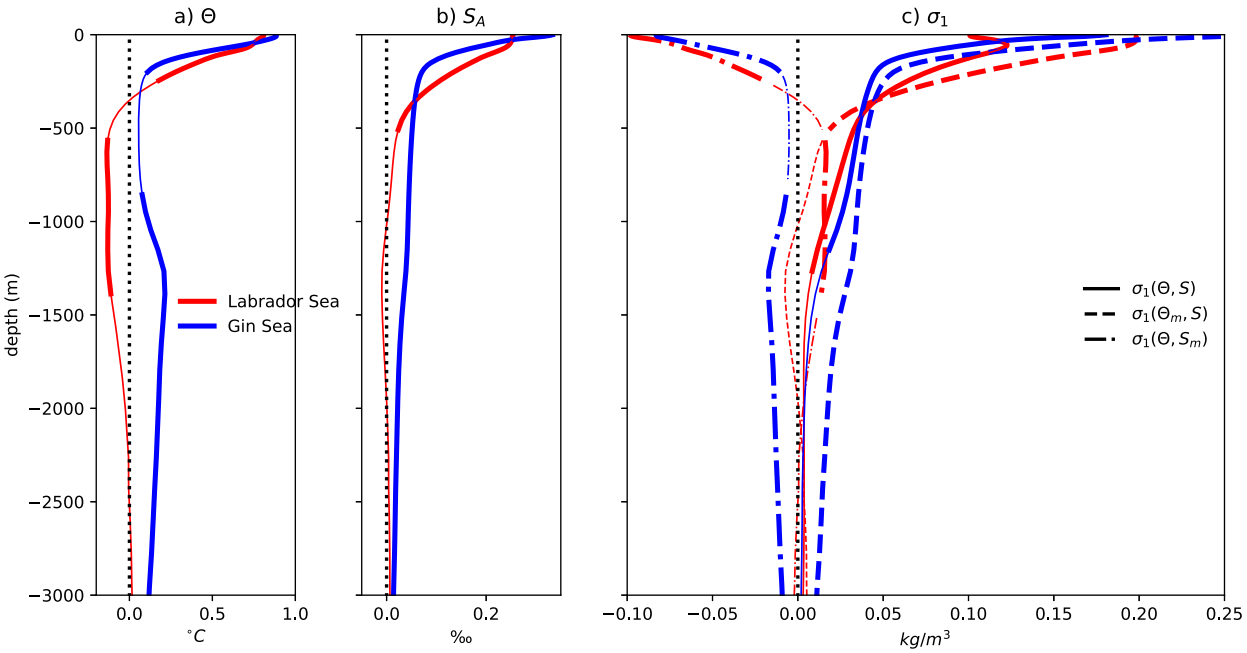

FIG. 9. Nine-year lead regression of the (a) Conservative Temperature Θ, (b) Absolute Salinity S_A, and (c) potential density at 1000 dbar σ_1 in the (red) Labrador Sea and (blue) GIN Seas onto the multidecadal AMOC PC1. Both regions are defined within the 9-yr lead MLD regression contour at 250 m. In (c), the density regression is decomposed into a saline contribution $\sigma_1(\Theta_m, S)$ (dashed) with Θ_m being the average temperature, and a thermal contribution $\sigma_1(\Theta, S_m)$ (dash–dotted) with S_m being the average salinity. Thick and thin line sections indicate that $p < 0.05$ and $p > 0.05$, respectively (Thomson and Emery 2014).

significantly, the Davis Strait overflow is both densified and intensified. Its location at the middepths in the northern edge of the Labrador Sea western boundary makes it a relevant driver of the AMOC centennial variability in CNRM-CM6. We are not aware of any previous study documenting the role of the Davis strait overflow as a driver of the AMOC low-frequency variability. At the Denmark Strait (Figs. 10c,d), the dominant features are: the East Greenland Current (EGC) advecting lighter water southward in the upper 300 m of the western boundary; the west Iceland current advecting denser waters northward in the upper 300 m of the eastern boundary; and the overflow advecting dense waters toward the Labrador Sea below 300-m depth. The regression onto the AMOC PC1 is dominated by the densification and weakening of the EGC. The west Iceland current is accelerated with no density anomalies. The overflow has a mostly insignificant velocity change and a weak densification. Therefore, it does not drive the centennial AMOC variability in CNRM-CM6. At the Iceland–Faroe (Figs. 10e,f) and Faroe–Scotland (Figs. 10g,h) channels, the upper 500 m circulation is dominated by the North Atlantic Current (NAC) entering the GIN Seas. The NAC extends down to 750-m depth in the Iceland–Faroe channel, whereas in the Faroe–Scotland channel, a dense water overflow is evident below 600-m depth. The regression onto the AMOC PC1 shows an intensification of both the NAC and the Faroe–Scotland dense water overflow. The density signal is weak to insignificant across both channels. The dense water overflow occurs along the eastern boundary of the subpolar gyre. Therefore, by thermal wind balance, its direct effect is to oppose the AMOC variability [see Eq. (23)]. In addition, a significant fraction of this transport can recirculate through the Iceland–Faroe channel. Although a fraction of this dense water could be advected toward the western boundary of the subpolar gyre, we conclude that the Iceland–Scotland channel is most likely not involved in the dense water variability that drives the AMOC low-frequency variability in CNRM-CM6. As a consequence, we found no causal link between the GIN Seas convection and the AMOC variability, although both strongly covary. The presence of an intense upper 500m saline anomaly preceding the AMOC PC1 in both the GIN and Labrador Seas suggests that both the GIN Seas convection and the AMOC low-frequency variability are driven by anomalous salinity advection toward the subpolar North Atlantic and the Nordic seas.

5. Conclusions

The aim of this work was twofold: to clarify the relation between the Atlantic meridional overturning circulation (AMOC) and the thermal wind balance and to investigate the strong centennial AMOC variability in a CMIP6-class model (CNRM-CM6). We have proposed a general framework that relates meridional oceanic transports outside the equator to densities at lateral boundaries. We stress the very generic nature of the formalism, which only requires a mass conservation constraint over the section of interest. The approach is not specific to one particular model nor to a specific time scale of variability and it could also be applied to interpret the observed

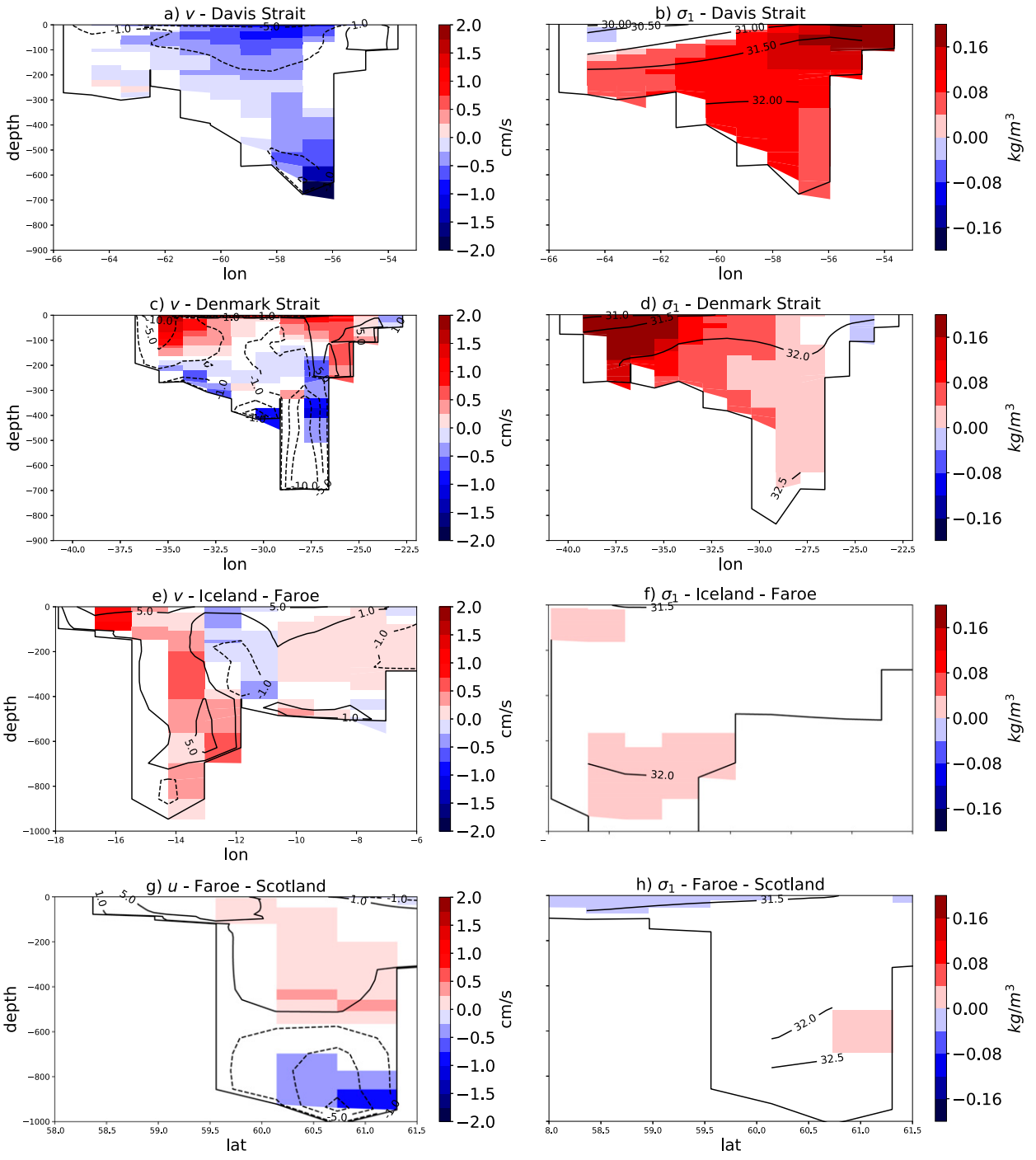

FIG. 10. Average (contours) and 9-yr lead regression (shades) of the (left) residual velocity exiting the subpolar gyre (cm s^{-1}) and (right) potential density at 1000 dbar σ_1 (kg m^{-3}) in the (a),(b) Davis Strait; (c),(d) Denmark Strait; (e),(f) Iceland–Faroe channel; and (g),(h) Faroe–Scotland channel onto the multidecadal AMOC PC1. Regions with $p > 0.05$ (Thomson and Emery 2014) are in white.

AMOC variability. The new mathematical formulation for the AMOC decomposition has permitted us to

- express the geostrophic shear component of the AMOC as a simple weighted vertical integral of densities at zonal boundaries,
- propose clear mathematical expressions for the external-mode AMOC transport arising from the effect of bottom velocities over zonally variable bathymetry,
- convert boundary density anomalies at any depth into a so-called thermal wind transport, in Sverdrups per meter, and

- predict that, for a typical Atlantic bathymetry of 4000 m and an AMOC upper-limb depth of 1000 m, a given boundary density anomaly induces most AMOC transport if it occurs in the 670–2000-m depth range.

Application to the low-frequency AMOC variability in the CNRM-CM6 climate model has shown the following:

- The CNRM-CM6 model has an intense centennial AMOC variability of period 150 years that is interhemispheric and propagates southward from northern subpolar latitudes.
- The new formulation for the AMOC reconstruction and specifically the geostrophic shear contribution explain over 80% of the multidecadal AMOC variance at all the latitudes considered, which hence results mostly from density anomalies at both zonal boundaries of the Atlantic Ocean.
- This geostrophic transport variability is largely explained by temperature anomalies at the western boundary of the North Atlantic, and to some extent by salinity anomalies at the eastern boundary of the South Atlantic.
- Converting density anomalies into a depth-dependent thermal wind transport (in Sverdrups per meter) reveals the dominant role of the 500–1500-m depth layer in setting the AMOC variability, in agreement with theoretical predictions.
- Although the top 500-m depth layer contribution largely correlates with the AMOC, the new AMOC formulation shows that this layer has a weak contribution to the AMOC variability.
- Interpretation of the AMOC variability in terms of individual thermohaline or boundary contributions is limited by the equation of state of seawater and the geostrophic relation, which allow large density-compensating thermohaline variations and covarying densities at both boundaries. This is particularly evident in the South Atlantic.

Investigation of the sources of the middepth density variability at the western boundary of the subpolar region reveals the driving role played by deep convection in the Labrador Sea and dense water overflow in the Davis Strait in the CNRM-CM6 model. The former has an intense variability along the western boundary of the Labrador Sea that precedes the AMOC variability by 9 years and produces cold and dense waters at middepths. The latter is located at the northern edge of the Labrador Sea western boundary and shows an enhanced dense water overflow that also leads the AMOC signal by several years. Deep convection variability is itself driven by an intense upper 500m salinity variability. Investigation of the causes of this near-surface salinity variability is left for a future study. Last, we found a strong covariance between the Greenland, Iceland, and Norwegian (GIN) Seas deep convection and the AMOC but with no clear mechanistic link between both: the GIN Seas deep convection does not appear necessary to explain the AMOC low-frequency variability in CNRM-CM6.

The thermal wind relation has illustrated the forcing of Atlantic Ocean dynamics by thermodynamics through the basin-integrated thermal pressure gradient force. A possible coupling could exist if the dynamics fed back onto the thermodynamics through anomalous heat and salinity advection by the AMOC. In that case the AMOC would be an active component of CNRM-CM6's centennial variability. Because of the dominance of the AMOC in setting the Atlantic Ocean meridional heat transport, it is plausible that such a coupling exists. In addition, the model's strong centennial sea surface temperature variability in the North Atlantic in response to the AMOC (Voldoire et al. 2019) suggests that a coupling mechanism could exist between the Atlantic Ocean and the atmosphere. Those feedback loops and their role in driving the low-frequency climate variability of the Atlantic region will be subject to a future work.

Acknowledgments. We thank two anonymous reviewers for their constructive and insightful comments that have greatly improved our paper. We also thank the CNRM-CM model development team for developing the CNRM-CM6 model and performing reference CMIP6 simulations and Hervé Giordani, Yohann Ruprich-Robert, Juliette Mignot, and Didier Swingedouw for fruitful discussions. This work was supported by the European Union's Horizon 2020 research and innovation program with the COMFORT project under Grant Agreement 820989 and the CONSTRAIN project under Grant Agreement 820829. Author J. Hirschi acknowledges funding from NERC, the NERC RAPID-AMOC project DYNAMOC (NE/M005097/1), and the NERC project ACSIS (NE/N018044/1).

REFERENCES

Baehr, J., J. Hirschi, J.-O. Beismann, and J. Marotzke, 2004: Monitoring the meridional overturning circulation in the North Atlantic: A model-based array design study. *J. Mar. Res.*, **62**, 283–312, https://doi.org/10.1357/0022240041446191.

Blanke, B., and P. Delecluse, 1993: Variability of the tropical Atlantic Ocean simulated by a general circulation model with two different mixed layer physics. *J. Phys. Oceanogr.*, **23**, 1363–1388, https://doi.org/10.1175/1520-0485(1993)023<1363:VOTTAO>2.0.CO;2.

Böning, C. W., A. Dispert, M. Visbeck, S. Rintoul, and F. U. Schwarzkopf, 2008: The response of the Antarctic circumpolar current to recent climate change. *Nat. Geosci.*, **1**, 864–869, https://doi.org/10.1038/ngeo362.

Borowski, D., R. Gerdes, and D. Olbers, 2002: Thermohaline and wind forcing of a circumpolar channel with blocked geostrophic contours. *J. Phys. Oceanogr.*, **32**, 2520–2540, https://doi.org/10.1175/1520-0485-32.9.2520.

Bryden, H. L., and S. Imawaki, 2001: Ocean heat transport. *Ocean Circulation and Climate*, G. Siedler, J. Church, and J. Gould, Eds., International Geophysics Series, Vol. 77, Academic Press, 455–474, https://doi.org/10.1016/S0074-6142(01)80134-0.

——, A. Mujahid, S. A. Cunningham, and T. Kanzow, 2009: Adjustment of the basin-scale circulation at 26°N to variations in Gulf Stream, deep western boundary current and Ekman transports as observed by the rapid array. *Ocean Sci.*, **5**, 421–433, https://doi.org/10.5194/os-5-421-2009.

Buckley, M. W., and J. Marshall, 2016: Observations, inferences, and mechanisms of the Atlantic Meridional Overturning Circulation: A review. *Rev. Geophys.*, **54**, 5–63, https://doi.org/10.1002/2015RG000493.

Cabanes, C., T. Lee, and L.-L. Fu, 2008: Mechanisms of interannual variations of the meridional overturning circulation of the

North Atlantic Ocean. *J. Phys. Oceanogr.*, **38**, 467–480, https://doi.org/10.1175/2007JPO3726.1.

Cassou, C., Y. Kushnir, E. Hawkins, A. Pirani, F. Kucharski, I.-S. Kang, and N. Caltabiano, 2018: Decadal climate variability and predictability: Challenges and opportunities. *Bull. Amer. Meteor. Soc.*, **99**, 479–490, https://doi.org/10.1175/BAMS-D-16-0286.1.

Chevallier, M., D. Salas y Mélia, A. Voldoire, M. Déqué, and G. Garric, 2013: Seasonal forecasts of the pan-arctic sea ice extent using a GCM-based seasonal prediction system. *J. Climate*, **26**, 6092–6104, https://doi.org/10.1175/JCLI-D-12-00612.1.

Clark, P., N. Pisias, T. Stocker, and A. Weaver, 2002: The role of the thermohaline circulation in abrupt climate change. *Nature*, **415**, 863–869, https://doi.org/10.1038/415863a.

Craig, A., S. Valcke, and L. Coquart, 2017: Development and performance of a new version of the OASIS coupler, OASIS3-MCT_3.0. *Geosci. Model Dev.*, **10**, 3297–3308, https://doi.org/10.5194/gmd-10-3297-2017.

Danabasoglu, G., 2008: On multidecadal variability of the Atlantic Meridional Overturning Circulation in the Community Climate System Model version 3. *J. Climate*, **21**, 5524–5544, https://doi.org/10.1175/2008JCLI2019.1.

de Lavergne, C., S. Falahat, G. Madec, F. Roquet, J. Nycander, and C. Vic, 2019: Toward global maps of internal tide energy sinks. *Ocean Modell.*, **137**, 52–75, https://doi.org/10.1016/j.ocemod.2019.03.010.

Decharme, B., and Coauthors, 2019: Recent changes in the ISBA-CTRIP land surface system for use in the CNRM-CM6 climate model and in global off-line hydrological applications. *J. Adv. Model. Earth Syst.*, **11**, 1207–1252, https://doi.org/10.1029/2018MS001545.

Desbruyères, D. G., H. Mercier, G. Maze, and N. Daniault, 2019: Surface predictor of overturning circulation and heat content change in the subpolar North Atlantic. *Ocean Sci.*, **15**, 809–817, https://doi.org/10.5194/os-15-809-2019.

Dong, B., and R. T. Sutton, 2005: Mechanism of interdecadal thermohaline circulation variability in a coupled ocean-atmosphere GCM. *J. Climate*, **18**, 1117–1135, https://doi.org/10.1175/JCLI3328.1.

Eyring, V., S. Bony, G. A. Meehl, C. A. Senior, B. Stevens, R. J. Stouffer, and K. E. Taylor, 2016: Overview of the Coupled Model Intercomparison Project Phase 6 (CMIP6) experimental design and organization. *Geosci. Model Dev.*, **9**, 1937–1958, https://doi.org/10.5194/gmd-9-1937-2016.

Fox-Kemper, B., R. Ferrari, and R. Hallberg, 2008: Parameterization of mixed layer eddies. Part I: Theory and diagnosis. *J. Phys. Oceanogr.*, **38**, 1145–1165, https://doi.org/10.1175/2007JPO3792.1.

Frankignoul, C., and K. Hasselmann, 1977: Stochastic climate models, Part II Application to sea-surface temperature anomalies and thermocline variability. *Tellus*, **29**, 289–305, https://doi.org/10.3402/tellusa.v29i4.11362.

——, P. Müller, and E. Zorita, 1997: A simple model of the decadal response of the ocean to stochastic wind forcing. *J. Phys. Oceanogr.*, **27**, 1533–1546, https://doi.org/10.1175/1520-0485(1997)027<1533:ASMOTD>2.0.CO;2.

Ganachaud, A., and C. Wunsch, 2003: Large-scale ocean heat and freshwater transports during the world ocean circulation experiment. *J. Climate*, **16**, 696–705, https://doi.org/10.1175/1520-0442(2003)016<0696:LSOHAF>2.0.CO;2.

Gastineau, G., and C. Frankignoul, 2012: Cold-season atmospheric response to the natural variability of the Atlantic meridional overturning circulation. *Climate Dyn.*, **39**, 37–57, https://doi.org/10.1007/s00382-011-1109-y.

Gent, P., and J. McWilliams, 1990: Isopycnal mixing in ocean circulation models. *J. Phys. Oceanogr.*, **20**, 150–155, https://doi.org/10.1175/1520-0485(1990)020<0150:IMIOCM>2.0.CO;2.

Hirschi, J., and J. Marotzke, 2007: Reconstructing the meridional overturning circulation from boundary densities and the zonal wind stress. *J. Phys. Oceanogr.*, **37**, 743–763, https://doi.org/10.1175/JPO3019.1.

——, J. Baehr, J. Marotzke, J. Stark, S. Cunningham, and J.-O. Beismann, 2003: A monitoring design for the Atlantic meridional overturning circulation. *Geophys. Res. Lett.*, **30**, 1413, https://doi.org/10.1029/2002GL016776.

Hughes, C. W., and P. D. Killworth, 1995: Effects of bottom topography in the large-scale circulation of the Southern Ocean. *J. Phys. Oceanogr.*, **25**, 2485–2497, https://doi.org/10.1175/1520-0485(1995)025<2485:EOBTIT>2.0.CO;2.

Jackson, L., and M. Vellinga, 2013: Multidecadal to centennial variability of the AMOC: HadCM3 and a perturbed physics ensemble. *J. Climate*, **26**, 2390–2407, https://doi.org/10.1175/JCLI-D-11-00601.1.

Johnson, H. L., and D. P. Marshall, 2002: A theory for the surface Atlantic response to thermohaline variability. *J. Phys. Oceanogr.*, **32**, 1121–1132, https://doi.org/10.1175/1520-0485(2002)032<1121:ATFTSA>2.0.CO;2.

Jungclaus, J. H., H. Haak, M. Latif, and U. Mikolajewicz, 2005: Arctic-North Atlantic interactions and multidecadal variability of the meridional overturning circulation. *J. Climate*, **18**, 4013–4031, https://doi.org/10.1175/JCLI3462.1.

Köhl, A., and D. Stammer, 2008: Variability of the meridional overturning in the North Atlantic from the 50-year GECCO state estimation. *J. Phys. Oceanogr.*, **38**, 1913–1930, https://doi.org/10.1175/2008JPO3775.1.

Kushnir, Y., 1994: Interdecadal variations in North Atlantic sea surface temperature and associated atmospheric conditions. *J. Climate*, **7**, 141–157, https://doi.org/10.1175/1520-0442(1994)007<0141:IVINAS>2.0.CO;2.

Lee, T., and J. Marotzke, 1998: Seasonal cycles of meridional overturning and heat transport of the Indian Ocean. *J. Phys. Oceanogr.*, **28**, 923–943, https://doi.org/10.1175/1520-0485(1998)028<0923:SCOMOA>2.0.CO;2.

Liu, Y., X. San Liang, and R. H. Weisberg, 2007: Rectification of the bias in the wavelet power spectrum. *J. Atmos. Oceanic Technol.*, **24**, 2093–2102, https://doi.org/10.1175/2007JTECHO511.1.

Lohmann, K., and Coauthors, 2014: The role of subpolar deep water formation and Nordic seas overflows in simulated multidecadal variability of the Atlantic meridional overturning circulation. *Ocean Sci.*, **10**, 227–241, https://doi.org/10.5194/os-10-227-2014.

Madec, G., and NEMO Team, 2016: NEMO ocean engine. Note du Pôle de modélisation de l'Institut Pierre-Simon Laplace 27, 386 pp., https://www.nemo-ocean.eu/wp-content/uploads/NEMO_book.pdf.NEMO ocean engine.

McCarthy, G., and Coauthors, 2015: Measuring the Atlantic meridional overturning circulation at 26°N. *Prog. Oceanogr.*, **130**, 91–111, https://doi.org/10.1016/j.pocean.2014.10.006.

Menary, M. B., D. L. R. Hodson, J. I. Robson, R. T. Sutton, and R. A. Wood, 2015: A mechanism of internal decadal Atlantic Ocean variability in a high-resolution coupled climate model. *J. Climate*, **28**, 7764–7785, https://doi.org/10.1175/JCLI-D-15-0106.1.

Msadek, R., and C. Frankignoul, 2009: Atlantic multidecadal oceanic variability and its influence on the atmosphere in a climate model. *Climate Dyn.*, **33**, 45–62, https://doi.org/10.1007/s00382-008-0452-0.

Muir, L. C., and A. V. Fedorov, 2015: How the AMOC affects ocean temperatures on decadal to centennial timescales: The North Atlantic versus an interhemispheric seesaw. *Climate Dyn.*, **45**, 151–160, https://doi.org/10.1007/s00382-014-2443-7.

——, and ——, 2017: Evidence of the AMOC interdecadal mode related to westward propagation of temperature anomalies in CMIP5 models. *Climate Dyn.*, **48**, 1517–1535, https://doi.org/10.1007/s00382-016-3157-9.

Nieves, D., and M. Spall, 2018: Propagation of North Atlantic deep water anomalies. *J. Phys. Oceanogr.*, **48**, 1831–1848, https://doi.org/10.1175/JPO-D-18-0068.1.

Olbers, D., D. Borowski, C. Völker, and J.-O. Wölff, 2004: The dynamical balance, transport and circulation of the Antarctic Circumpolar Current. *Antarct. Sci.*, **16**, 439–470, https://doi.org/10.1017/S0954102004002251.

Ortega, P., M. Montoya, F. González-Rouco, J. Mignot, and S. Legutke, 2012: Variability of the Atlantic meridional overturning circulation in the last millennium and two IPCC scenarios. *Climate Dyn.*, **38**, 1925–1947, https://doi.org/10.1007/s00382-011-1081-6.

——, J. Robson, R. T. Sutton, and M. B. Andrews, 2017: Mechanisms of decadal variability in the Labrador Sea and the wider North Atlantic in a high-resolution climate model. *Climate Dyn.*, **49**, 2625–2647, https://doi.org/10.1007/s00382-016-3467-y.

Rayner, D., and Coauthors, 2011: Monitoring the Atlantic meridional overturning circulation. *Deep-Sea Res. II*, **58**, 1744–1753, https://doi.org/10.1016/j.dsr2.2010.10.056.

Redi, M. H., 1982: Oceanic isopycnal mixing by coordinate rotation. *J. Phys. Oceanogr.*, **12**, 1154–1158, https://doi.org/10.1175/1520-0485(1982)012<1154:OIMBCR>2.0.CO;2.

Roberts, C. D., F. K. Garry, and L. C. Jackson, 2013: A multimodel study of sea surface temperature and subsurface density fingerprints of the Atlantic meridional overturning circulation. *J. Climate*, **26**, 9155–9174, https://doi.org/10.1175/JCLI-D-12-00762.1.

Ruprich-Robert, Y., and C. Cassou, 2015: Combined influences of seasonal east Atlantic pattern and North Atlantic oscillation to excite Atlantic multidecadal variability in a climate model. *Climate Dyn.*, **44**, 229–253, https://doi.org/10.1007/s00382-014-2176-7.

Saenko, O. A., J. C. Fyfe, and M. H. England, 2005: On the response of the oceanic wind-driven circulation to atmospheric CO_2 increase. *Climate Dyn.*, **25**, 415–426, https://doi.org/10.1007/s00382-005-0032-5.

Séférian, R., and Coauthors, 2019: Evaluation of CNRM earth system model, CNRM-ESM2-1: Role of earth system processes in present-day and future climate. *J. Adv. Model. Earth Syst.*, **11**, 4182–4227, https://doi.org/10.1029/2019MS001791.

Sime, L. C., D. P. Stevens, K. J. Heywood, and K. I. C. Oliver, 2006: A decomposition of the Atlantic meridional overturning. *J. Phys. Oceanogr.*, **36**, 2253–2270, https://doi.org/10.1175/JPO2974.1.

Stocker, T. F., 1998: The seesaw effect. *Science*, **282**, 61–62, https://doi.org/10.1126/science.282.5386.61.

Taylor, K. E., 2001: Summarizing multiple aspects of model performance in a single diagram. *J. Geophys. Res.*, **106**, 7183–7192, https://doi.org/10.1029/2000JD900719.

Thomson, R. E., and W. J. Emery, 2014: Statistical methods and error handling. *Data Analysis Methods in Physical Oceanography*, 3rd ed. R. E. Thomson, and W. J. Emery, Eds., Elsevier, 219–311, https://doi.org/10.1016/B978-0-12-387782-6.00003-X.

Torrence, C., and G. P. Compo, 1998: A practical guide to wavelet analysis. *Bull. Amer. Meteor. Soc.*, **79**, 61–78, https://doi.org/10.1175/1520-0477(1998)079<0061:APGTWA>2.0.CO;2.

Trenberth, K. E., and J. T. Fasullo, 2017: Atlantic meridional heat transports computed from balancing Earth's energy locally. *Geophys. Res. Lett.*, **44**, 1919–1927, https://doi.org/10.1002/2016GL072475.

Tulloch, R., and J. Marshall, 2012: Exploring mechanisms of variability and predictability of Atlantic meridional overturning circulation in two coupled climate models. *J. Climate*, **25**, 4067–4080, https://doi.org/10.1175/JCLI-D-11-00460.1.

Vellinga, M., and P. Wu, 2004: Low-latitude freshwater influence on centennial variability of the Atlantic thermohaline circulation. *J. Climate*, **17**, 4498–4511, https://doi.org/10.1175/3219.1.

Voldoire, A., and Coauthors, 2013: The CNRM-CM5.1 global climate model: Description and basic evaluation. *Climate Dyn.*, **40**, 2091–2121, https://doi.org/10.1007/s00382-011-1259-y.

——, and Coauthors, 2019: Evaluation of CMIP6 deck experiments with CNRM-CM6-1. *J. Adv. Model. Earth Syst.*, **11**, 2177–2213, https://doi.org/10.1029/2019MS001683.

Yeager, S. G., and J. I. Robson, 2017: Recent progress in understanding and predicting Atlantic decadal climate variability. *Curr. Climate Change Rep.*, **3**, 112–127, https://doi.org/10.1007/s40641-017-0064-z.

Zhang, R., R. Sutton, G. Danabasoglu, Y.-O. Kwon, R. Marsh, S. G. Yeager, D. E. Amrhein, and C. M. Little, 2019: A review of the role of the Atlantic Meridional Overturning Circulation in Atlantic Multidecadal Variability and associated climate impacts. *Rev. Geophys.*, **57**, 316–375, https://doi.org/10.1029/2019RG000644.